UNIVERSIDADE DA CORUÑA

E.T.S. DE INGENIEROS DE CAMINOS,
CANALES Y PUERTOS
A CORUÑA

Proyecto técnico:

TWO-DIMENSIONAL UNSTEADY TURBULENCE MODELLING IN FREE SURFACE SHALLOW WAKES

Author: Pablo Ouro Barba

Supervised by: Luis Cea Gómez

Agradecimientos

Quiero mostrar mi agradecimiento a un gran número de personas que me han ayudado y apoyado durante la realización de este proyecto.

En primer lugar, agradecer a mi tutor Luis Cea por su gran ayuda incondicional, por su inmensa paciencia y por haberme dado la oportunidad de realizar un proyecto de investigación de esta magnitud.

A mis compañeros de carrera, por todos los buenos momentos que durante estos años hemos compartido. En especial, a Luis Ramírez por su gran apoyo desde el primer momento. También a mi amigos Adrián, Juan, Isa, Pachu, Javi y Jose por su amistad y comprensión.

Gran parte de este proyecto se ha realizado durante mi estancia como Erasmus en Suecia, por lo que agradezco a mis amigos Damien y Mathieu por sus consejos en la modelización CFD y en el análisis de datos. Además a Francesca, Yago, Maciek, Marine, Rui, y Subi por la gran experiencia que pasamos juntos.

A mi familia por toda su ayuda. A mis padres y a mi hermano, que les debo todo, por darme todo el apoyo que necesité en este proyecto y en toda la carrera. Sin embargo, me gustaría agradecer de forma especial el apoyo de mis abuelos ya que sin ellos no sería posible realizar nada de esto.

Por último, agradecer a mi novia, Yanina Sánchez por su cariño y apoyo en los momentos duros de este proyecto, y que sin ello no habría podido culminarlo.

Acknowledgments

I would like to send out my gratitude to all those people that have helped and supported me during this project.

First of all, I would like to give appreciation to my tutor Luis Cea the unconditional help, immense pacience and having given me the opportunity to carry out this MSc project.

To my university mates, thank you for all those good moments we spent together along these years. Specially, thanks to Luis Ramírez for his huge support since the first moment. Also thanks to my good friends Adrián, Juan, Pachu, Javi and Jose for their friendship and comprehension.

Most of this project was carried out in Sweden when I was an Erasmus student at Chalmers University. Therefore, I really appreciate the help that Mathieu and Damien offered me in the CFD simulations and in the data analysis. Also I want to thank Francesca, Yago, Maciek, Marien, Rui and Subi for the experience we spent together.

To my family, my parents and my brother, as they gave me the chance to complete the degree and who supported me completely along the way with this project. However, I would like to give special appreciation to my grandparents from whom I received a huge amount of support as without them none of this success could be achieved.

Finally, I would like to give thank my girlfriend, Yanina Sánchez for her love and unconditional support in the hard moments of this project as it probably could not have been finished without her.

MEMORIA

Introducción

La modelización de aguas someras es un campo de ingeniería hoy en día en auge. El número de aplicaciones es muy grande y se pueden destacar la modelización de flujos en estuarios, ríos, flujo alrededor de pilas de puentes, diques marinos, etc. Para el análisis de este campo de la mecánica de fluidos computacional (CFD), se utilizan las ecuaciones de flujo en aguas someras. Estas ecuaciones provienen de las ecuaciones de Navier-Stokes, junto con una serie de hipótesis para adaptar a las características de estos flujos, como el promedio de resultados en calado.

En aguas someras, los flujos son fundamentalmente turbulentos. Por ello, la modelización de la turbulencia en CFD es muy importante. Este proyecto de investigación se centra en estudiar diferentes formas de modelizar de estos fenómenos turbulentos. Para ello se utilizan varios esquemas numérico, para prevenir una elevada difusión en los resultados, y varios modelos de turbulencia. Dentro de estos modelos de turbulencia, se utilizan dos modelos que resuelven una mayor cantidad de energía que modelos tradicionales, permitiendo acercar más los resultados de las simulaciones a los experimentales.

Metodología

Para resolver las ecuaciones de aguas someras se ha utilizado un código en con volúmenes finitos, ya que es la técnica más utilizada en la resolución de problemas en CFD. Debido a las propiedades de las aguas someras, las ecuaciones utilizadas tienen un carácter bidimensional, utilizando un promedio según el calado. Para la verificación del modelo se comparan resultados experimentales con simulaciones numéricas.

Se han utilizado en las simulaciones varios esquemas numéricos diferenciados por su mayor o menos difusividad. Los flujos analizados son flujos de agua alrededor de una placa plana y de un cilindro. Los modelos de turbulencia más comúnmente utilizados en estos problemas son los tipo RANS (Reynolds Averaged Navier Stokes). En este proyecto, se propone el análisis de nuevos modelos de turbulencia tipo PANS (Partially Averaged Navier-Stokes) y filter-based RANS. Estos modelos representan una novedad en modelización de flujos en aguas someras y se utilizan para aumentar la cantidad de turbulencia resuelta por el modelo numérico. Estos dos métodos se basan en un sistema de filtrado parcial basado en el porcentaje de la cantidad de energía cinética turbulenta resuelta en el caso de PANS y en el tamaño mínimo de las inestabilidades resueltas en filter-based RANS. Estos métodos, dotados de una malla suficientemente refinada, tienden a una simulacion tipo LES. La ventaja de estos métodos es el tiempo computacional que es mucho menor que el utilizado en una simulación tipo LES. Los resultados se centran en el análisis de los términos de energía cinética resuelta y modelada, campos de velocidades, disipación y frecuencia de los vórtices.

Conclusiones

Los resultados de las modelizaciones con CFD concuerdan de manera satisfactoria con los resultados experimentales. En el flujo alrededor de la placa plana, las simulaciones reproducen correctamente todas las inestabilidades. En cuanto al cilindro, las simulaciones con CFD utilizando un esquema numérico de Roe y el modelo de turbulencia $k-\varepsilon$ de Rastogi y Rodi, los resultados muestran problemas cuando el número de Froude es bajo.

La influencia del esquema numérico utilizado es tan influyente en los resultados como el modelo de turbulencia. De los resultados se concluye que los esquemas HLLCC y Upwind-HLL simulan un mayor grado de turbulencia al no amortiguar tanto las inestabilidades como los esquemas que introducen una mayor difusión numérica, entre ellos Roe.

En cuanto a los modelos de turbulencia, los modelos de PANS y filter-based URANS muestran resultados diferentes respecto a las simulaciones de URANS, presentando un mayor nivel de turbulencia en filter-based URANS. Los filtros que resuelven una mayor cantidad de energía turbulenta (f_k entre 0.4 y 0.2; $\triangle$ con un valor cercano al tamaño de elemento de la malla), lo hacen en las zonas donde ésta es imporante, como en las zonas tras el cilindro donde los vórtices se crean y se desprenden. El modelo filter-based URANS, utilizando un filtro muy pequeño, es capaz de reproducir inestabilidades de pequeña escala, lo cual no es observado en los otros modelos.

Contents

List of Figures

List of Tables

Introduction

The study of the flow around bluff bodies in many engineering fields, as enviromental, ocean or hydraulic engineering, has been of interest for many decades. In enviromental engineering, how the wind flow provokes a Von Kármán street due to the interaction with islands, (Fig. 0.1(a)), or even the sea water flow across an island (Fig. 0.1(b)), is of interest to many researchesr [9]. In hydraulic engineering the application of numerical models is used for incompressible flow, open channels, free surface flow, etc. Flow modelling in open channel helps to improve out on the knowledge on the flow generated around surface piercing cylinders, esential in bridge design, flow around submerged bluff bodies regarding fish habitat structures and water intakes, etc. Thus, to develop numerical methods that efficiently model these flows is a need.

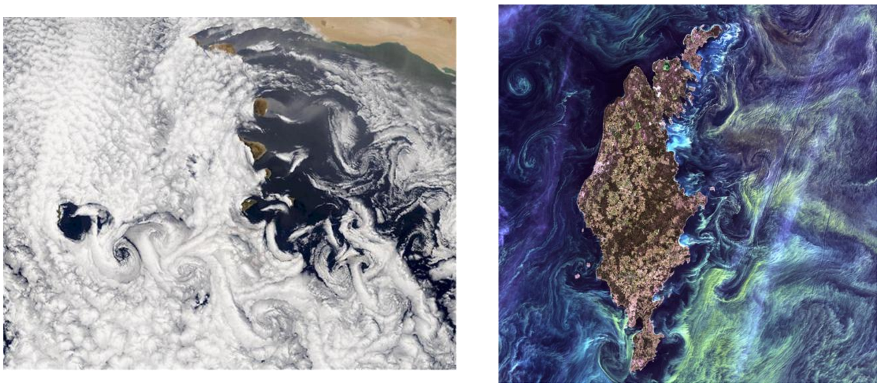

(a) Von Kármán street observed at the Canary Islands, Spain.

(b) Vortex formation in the sea water observed at the Gotland Island, Sweden.

Figure 0.1: Island wakes examples

Almost all the free surface flows are turbulent, so the CFD model has to be chosen properly depend on the flow characteristics. There are many shallow water flow phenomena that are modelled with 3D models but their computational cost is very high. However, there are other flows for which two-dimensional models can be used with a good accuracy. These models applied to shallow water flows are denoted as 2D Shallow Water Equations. The equations used in this model use a depth averaged approach.

The level of turbulence in shallow water flows makes it necessary to use models that simulates properly the turbulent stresses. In this work, there are presented two recent approaches in the shallow water flow turbulence modelling around bluff bodies. Two low diffusion numerical schemes are compared with standard numerical schemes used in shallow waters flow that have a higher numerical diffusion. On the other hand, the turbulence modelling simulations are made with two turbulence models, based in RANS equations, that apply turbulence filtering, as PANS and filter-based URANS. Both the numerical schemes and the turbulence models are compared with more standard models.

Chapter 1

1 Fundamental equations of turbulent flow

1.1 Fundamental equations

In fluid dynamics, the characteristic equations are the continuity equation and the momentum equation. The continuity equation is based in the physical principle: *the mass is conserved.* Eq. 1.1 represents the continuity equation:

$$\frac{D\rho}{Dt} + \rho[\nabla\vec{V}] = 0 \tag{1.1}$$

The momentum equation is based in Newton's Second Law, $F{=}m \cdot a$. Considering a fluid element, this physical principle stablishes that the net force on the fluid element equals its mass times its acceleration. The force experienced by the fluid element can be done by two different sources:

a. **Body forces**. Act directly on the volumetric mass of the fluid element. These forces act *at a distance* as gravity, magnetic or electric forces.

b. **Surface forces**. Act on the surface of the fluid element. These can be clasified in two sources:

   I) The pressure (p) distribution acting on the surface, due to the outside fluid surrounding the fluid element.

   II) The shear and normal stresses (τ_{ij}) acting on the surface, imposed by the outside fluid by terms of friction.

The momentum equations are presented in Eq. 1.2.

$$\begin{aligned}
\frac{\partial(\rho u)}{\partial t} + \nabla\cdot(\rho u\vec{V}) &= (-\frac{\partial p}{\partial x} + \frac{\partial \tau_{xx}}{\partial x} + \frac{\partial \tau_{yx}}{\partial y} + \frac{\partial \tau_{zx}}{\partial z}) + \rho f_x \\
\frac{\partial(\rho v)}{\partial t} + \nabla\cdot(\rho v\vec{V}) &= (-\frac{\partial p}{\partial y} + \frac{\partial \tau_{xy}}{\partial x} + \frac{\partial \tau_{yy}}{\partial y} + \frac{\partial \tau_{zy}}{\partial z}) + \rho f_y \\
\frac{\partial(\rho w)}{\partial t} + \nabla\cdot(\rho w\vec{V}) &= (-\frac{\partial p}{\partial z} + \frac{\partial \tau_{xz}}{\partial x} + \frac{\partial \tau_{yz}}{\partial y} + \frac{\partial \tau_{zz}}{\partial z}) + \rho f_z
\end{aligned} \tag{1.2}$$

The continuity equation (Eq. 1.1) and the momentum equation in the three directions (Eq. 1.2) are the main equations in fluid dynamics. They are known as *Navier-Stokes equations.* Considering a constant density, these equations are written in tensorial form as:

$$\frac{\partial u_j}{\partial x_j} = 0 \tag{1.3}$$

$$\frac{\partial u_i}{\partial t} + \frac{\partial u_i u_j}{\partial x_j} = -\frac{1}{\rho}\frac{\partial p}{\partial x_i} + \frac{1}{\rho}\frac{\partial \tau_{ij}}{\partial x_j} + F_i$$

A fluid dynamic problem can be solved by these equations directly. This method is called *Direct Numerical Simulation (DNS).* It needs an enormous computational capacity to achieve good results in turbulent flows. Thus, only in very simple problems this can be done. In the following, some numerical approaches that reduces this difficulty are presented.

1.2 Reynolds Averaged Navier-Stokes (RANS)

The Reynolds Averaged Navier-Stokes (RANS) equation is focused on the mean flow and the effects of turbulence on the mean flow properties. In RANS, the Navier-Stokes equations are time averaged, the instantaneous velocity is decomposed into a mean value ($\bar{u}$) and a fluctuation value (*u'*). This is called the *Reynolds decomposition.*

$$u_i = \bar{u}_i + u_i' \tag{1.4}$$

This decomposition is introduced in the continuity equation and momentum equations (Eq. 1.3). The resulting fundamental RANS equation is:

$$\frac{\partial \bar{u}_i}{\partial t} + \bar{u}_j\frac{\partial \bar{u}_i}{\partial x_j} = -\frac{1}{\rho}\frac{\partial p}{\partial x_i} + \nu\frac{\partial^2 \bar{u}_i}{\partial {x_j}^2} - \frac{\partial \overline{u_i' u_j'}}{\partial x_j} \tag{1.5}$$

The first term on the right-side equation terms corresponds to the pressure gradient. The second is related with the viscous stresses and the last one are the turbulent stresses. These last terms appear in the time-averaged flow equations due to the interactions between turbulent fluctuations.

Regard to model turbulence with the RANS equations there are multiple models. It can be mainly distinguished four types of turbulence models depending on the number of equations they solve:

a. **Algebraic models**.

An algebraic equation is used to compute a turbulent viscosity, also called *eddy viscosity*, μ_t. The Reynolds stress tensor ($\overline{u_i' u_j'}$) from RANS equations (Eq. 1.5) is computed using an assumption which relates the Reynolds stress tensor to the velocity gradients and the turbulent viscosity. This assumption is the so-called *Boussinesq assumption.* Boussinesq proposed that Reynolds stresses might be proportional to the mean rates of deformation:

$$\overline{u_i' u_j'} = -\nu_t \left(\frac{\partial \overline{u_i}}{\partial x_j} + \frac{\partial \overline{u_j}}{\partial x_i} \right) - \frac{2}{3} k \delta_{ij} \tag{1.6}$$

where δ_{ij} is the Kronecker delta and k is the modelled kinetic energy.

b. **One-equation models**.

   These models are also based on Boussinesq assumption. One transport equation is solved for a turbulent quantity (as kinetic energy) in order to compute the eddy viscosity. The *Spalart-Allmaras model* is an example of these models.

c. **Two-equation models**.

   Two transport equations are solved, describing two scalars, for example the turbulent kinetic energy k and the dissipation ε. The Reynolds stress tensor is computed with the Boussinesq assumption. Models as *k-ω model*, *k-τ model* or *k-ε model* are some of the most used.

d. **Reynolds Stress Models**

   A transport equation is derived for the Reynolds tensor, $\overline{u_i' u_j'}$. One transport equation has to be added for determining the length scale of turbulence. Regarding the dissipation ε, another equation is used for its calculation.

The complexity of these models advance from the easiest up to the hardest (RSM). This increasing difficulty is due to the computational cost, because for the RSM six extra partial differential equations have to be solved.

1.3 Turbulence characteristics

The turbulent flow has a chaotic and random behaviour with several characteristic properties. The main characteristics are [4]:

a. **Irregularity**. Turbulent flow is irregular, random and chaotic. Even though this irregularity, it can be well-described by the Navier-Stokes equations.

b. **Diffusivity**. In turbulent flow the diffusivity increases. This means that the spreading rate of boundary layers increases as the flow becames turbulent.

c. **Three-dimensional**. Turbulence flow is a three-dimensional phenomenon. However it can be modelled as two-dimensional in cases as shallow water flows.

d. **Dissipation**. A turbulent flow is dissipative. The kinetic energy from the small eddies is transformed, due to this dissipation, into internal energy following the *cascade process.*

e. **Continuum**. The considered small turbulent scales are much larger than the molecular scale, what allows to treat the flow as a continuum.

The visualization of turbulent flows reveals rotational flow structures, so-called turbulent eddies, with a wide range of length scales. *The cascade process* explains the mechanisms on a turbulent flow.

The turbulent flow is analyzed in multiple ways in this document. There are several parameters that characterizes the analysis of a turbulent flow. These are the turbulent kinetic energy, the dissipation, rate of turbulence and hydrodynamic coefficients.

1.3.1 Kinetic energy

Every turbulence modelling approach models the kinetic energy and dissipation in a different way. It is interesting to study how different the results are, depending on the model used. This section explains how and why the kinetic energy is obtained in several ways.

a. **Modelled kinetic energy**, k_m. In the RANS equations, the Reynolds stresses are modelled. Considering the normal direction terms $u_1'u_1'$, $u_2'u_2'$ and $u_3'u_3'$, the modelled kinetic energy is obtained as:

$$k_m = \frac{\overline{u_1'^2} + \overline{u_2'^2} + \overline{u_3'^2}}{2} \tag{1.7}$$

b. **Resolved kinetic energy**, k_r. This term represents the turbulence fluctuation. It indicates the variance of the velocity fluctuations in time.

c. **Total kinetic energy**, k_t. The total kinetic energy value is the summation of the modelled kinetic energy and the resolved kinetic energy, as $k_t = k_r + k_m$.

1.3.2 Dissipation (ε)

This term is responsible for the transformation of kinetic energy at small scales to thermal energy. The small eddies receive the kinetic energy from slightly larger eddies. This ones receive their energy from even larger eddies and so on, following *energy cascade process.*

The large eddies are dominated by inertia effects and viscous effects are negligible, meaning that the large eddies are mostly inviscid. In the *cascade process*, the large eddies extract the *kinetic energy* from the mean flow, which is transferred via smaller and smaller eddies down to the smallest eddies. In the smallest scales the kinetic energy is transformed into internal energy (as thermal energy), increasing the temperature. This last process is called *dissipation* and it is denoted as ε $[m^2/s^3]$. Whereas the large scales, which interact with the mean flow, have an orientation imposed by the mean flow, it is usually assumed that the small scales forget the structure and orientation of the large scales having an undefined movement. Thus, the smallest scales are *isotropic*, independent of the direction.

Fig. 1.1 shows the energy spectrum. This represents the energy distribution of turbulent kinetic energy over the different turbulent scales, from the large scales dominated by the mean flow down to the smallest scales where the dissipation takes place.

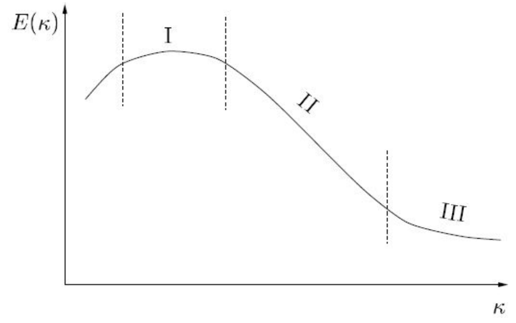

Figure 1.1: Energy spectrum. From [4]

In Fig. 1.1 there are three different zones. The first (I) is the large eddies region which take most of the energy. Their energy is transferred to the small eddies along the transition region (II), which is denoted as *inertial range*. Finally, the last region (III), named as *dissipation range* is where the vortices lose their energy and it is transformed into thermal energy due to the dissipation.

1.3.3 Hydrodynamic coefficients

In addition to turbulent kinetic energy and dissipation, it is common to use hydrodynamic coefficients that help to analyze the data from simulations. These are the lift and drag coefficients. These are calculated from the force that the water makes over a body, which is divided in pressure force and friction force. The pressure force is the component perpendicular to the surface of the body, and the friction is the parallel one.

Lift coefficient

It is calculated from the y-component of the force, which is the perpendicular to the income flow direction. The expression of this coefficient is:

$$C_L = \frac{F_y}{\frac{1}{2}\rho U^2 A} \tag{1.8}$$

where F_y is sum of the pressure and friction forces in y-direction, ρ is the fluid density, U is the fluid velocity and A is the projected area

Drag coefficient

It is analogous to the lift coefficient but in this case, the considered force is the x-direction components. It is calculated as:

$$C_D = \frac{F_x}{\frac{1}{2}\rho U^2 A} \tag{1.9}$$

where F_x is sum of the pressure and friction forces in x-direction.

1.4 Turbulence models

In many engineering CFD simulations with RANS, the k-ε model is used in order to model turbulence. In addition to RANS, PANS and filter-based RANS are also other models used in this work.

1.4.1 k-ε model

The $k-\varepsilon$ model is often used in fluid flow modelling and there is a large amount of bibliography, see [5] or [12] among others. In this model, the eddy viscosity is computed as:

$$\nu_t = C_\mu \frac{k^2}{\varepsilon} \tag{1.10}$$

The standard transport equations for k and ε are:

$$\frac{\partial k}{\partial t} + \frac{\partial \bar{u}_j k}{\partial x_j} = \frac{\partial}{\partial x_j}\left[\left(\nu + \frac{\nu_t}{\sigma_k}\right)\frac{\partial k}{\partial x_j}\right] + P_k - \varepsilon \tag{1.11}$$

$$\frac{\partial \varepsilon}{\partial t} + \frac{\partial \bar{u}_j \varepsilon}{\partial x_j} = \frac{\partial}{\partial x_j}\left[\left(\nu + \frac{\nu_t}{\sigma_\varepsilon}\right)\frac{\partial \varepsilon}{\partial x_j}\right] + C_{\varepsilon_1} P_k \frac{\varepsilon}{k} - C_{\varepsilon_2}\frac{\varepsilon^2}{k} \tag{1.12}$$

The term P_k is the production term of the turbulent kinetic energy. It is calculated as:

$$P_k = \nu_t(\frac{\partial \bar{u}_i}{\partial x_j} + \frac{\partial \bar{u}_j}{\partial x_i})\frac{\partial \bar{u}_i}{\partial x_j} \tag{1.13}$$

Finally the five constant present in these equations have the following values:

$$C_\mu = 0.09 \quad \sigma_k = 1.00 \quad \sigma_\varepsilon = 1.30 \quad C_{1\varepsilon} = 1.44 \quad C_{2\varepsilon} = 1.92$$

1.4.2 Partially Averaged Navier-Stokes equations (PANS)

The PANS model tries to resolve the largest turbulent scales. The PANS model is a *hybrid model* that combines desirable properties of RANS and LES. In PANS, a filter is used to control by specifying the desired levels of unresolved-to-total kinetic energy ratio, f_k, and the unresolved-to-total dissipation ratio, f_ε. The resolved turbulent kinetic energy is larger as the f_k ratio becomes smaller. These ratios are defined as:

$$f_k = \frac{k_u}{k} \qquad\qquad f_\varepsilon = \frac{\varepsilon_u}{\varepsilon} \tag{1.14}$$

where k_u is the unresolved partially averaged turbulent kinetic energy, k is the total turbulent kinetic energy, ε_u is the unresolved partially averaged dissipation and ε is the total dissipation.

Both ratios have a range of values between 0 and 1. Physically f_k must be less or equal to f_ε, due to the fact that large scales (typically resolved) contain most of the kinetic energy whereas the dissipation occurs mostly in small scales (which are typical unresolved). PANS approaches DNS as f_k approaches zero, providing that the numerical mesh is fine enough to resolve the dissipative turbulent scales. On the other hand, when its value approaches 1, the model converges to the RANS solution.

In the following, the standard PANS equations proposed by Girimaji [13] are presented:

$$\frac{\partial k_u}{\partial t} + \frac{\partial \bar{u}_j k_u}{\partial x_j} = \frac{\partial}{\partial x_j}\left[\left(\nu + \frac{\nu_u}{\sigma_{ku}}\right)\frac{\partial k_u}{\partial x_j}\right] + P_u - \varepsilon_u \tag{1.15}$$

$$\frac{\partial \varepsilon_u}{\partial t} + \frac{\partial \bar{u}_j \varepsilon_u}{\partial x_j} = \frac{\partial}{\partial x_j}\left[\left(\nu + \frac{\nu_u}{\sigma_{\varepsilon_u}}\right)\frac{\partial \varepsilon_u}{\partial x_j}\right] + C_{\varepsilon_1} P_u \frac{\varepsilon_u}{k_u} - C^*_{\varepsilon_2}\frac{\varepsilon_u^2}{k_u} \tag{1.16}$$

The constant $C^*_{\varepsilon_2}$ is given by:

$$C^*_{\varepsilon_2} = \frac{f_k}{f_\varepsilon}(C_{\varepsilon 1} - C_{\varepsilon 2}) + C_{\varepsilon 1} \tag{1.17}$$

The Prandtl numbers are given by:

$$\begin{aligned} \sigma_{ku} &= \sigma_k \cdot f_k^2/f_\varepsilon \\ \sigma_{\varepsilon u} &= \sigma_\varepsilon \cdot f_k^2/f_\varepsilon \end{aligned} \tag{1.18}$$

The production term used in this method is P_u, which is defined as:

$$P_u = \nu_u \left(\frac{\partial \bar{u}_i}{\partial x_j} + \frac{\partial \bar{u}_j}{\partial x_i} \right) \frac{\partial \bar{u}_i}{\partial x_j} \tag{1.19}$$

The total turbulent eddy viscosity ν_t can be computed from the unresolved eddy viscosity ν_u and the ratios f_k and f_ε:

$$\nu_u = C_\mu \frac{k_u^2}{\varepsilon_u} \tag{1.20}$$

$$\nu_t = \frac{f_\varepsilon}{f_k^2} \cdot \nu_u \tag{1.21}$$

Finally, there are five model constant which take the same value as in the standard $k - \varepsilon$ model:

$$C_\mu = 0.09 \quad \sigma_k = 1.40 \quad \sigma_\varepsilon = 1.30 \quad C_{\varepsilon_1} = 1.50 \quad C_{\varepsilon_2} = 1.90$$

1.4.3 Filter-based URANS

As PANS, this model is an hybrid between LES and RANS. The equations used to model turbulence are the $k - \varepsilon$ equations with a spatial filter to evaluate the turbulent viscosity.

The idea is to reduce the effective viscosity used in the model in order to offer more satisfactory resolutions of the largest turbulent eddies. By imposing a filter on the turbulence model, those turbulent structures smaller than the filter size will not be resolved. In terms of resolved turbulent kinetic energy, this is larger as the filter size is smaller. When this filter size is set to values smaller than the length scales returned by the conventional RANS models, the computation will allow for the development of flow structures within the resolution capability of the combination of the chosen turbulent closure, numerical scheme and grid size.

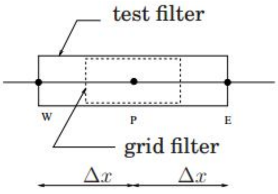

Figure 1.2: Filter size representation

A desired filter size ($\triangle_{preset}$) is imposed by the modeller. However, the computed filter size is a function of this preset filter and the mesh size (see Fig. 1.2). Indeed if the mesh is very coarse, it can dominate the filter size. Eq. 1.22 shows how filter size, is computed:

$$\begin{aligned} \triangle &= max[\triangle_{preset}, \triangle_{grid}] \\ \triangle_{grid} &= [\triangle_x \cdot \triangle_y]^{1/2} \end{aligned} \tag{1.22}$$

The developed governing equations are presented by Johansen [14]. The eddy viscosity expression with this model is computed as:

$$\nu_t = C_\mu f \frac{k^2}{\varepsilon} \tag{1.23}$$

where the function f depends on the filter size:

$$f = min[1, \frac{\triangle\varepsilon}{k^{3/2}}] \tag{1.24}$$

Chapter 2

2 Turbulent flow in shallow waters

The turbulence is a feature of the flow not of the fluid. A turbulent flow is characterized by a *Reynolds number* (Eq. 2.1) above the value called critical Reynolds number which stablishes the transition from laminar to turbulent flow. The Reynolds number is defined as:

$$Re = \frac{H \cdot U}{\nu} \tag{2.1}$$

where H is the length scale, U is the velocity scale and ν is the kinematic viscosity. Usually just the Reynolds number is used to characterize how the water flow behaves, for example across a bluff body.

2.1 Shallow water flow

When water flow with free surface is modelled, the ratio between the water depth H and the body length L determines the equations to be used. In shallow water flow this ratio has a value much lower than the unit. In most of fluid flow cases the characteristic parameter is the *Reynolds number*. However, the shallow water flows are also charactericed by the *shallow wake parameter*, defined as [8]:

$$S = C_f \cdot D/H \tag{2.2}$$

where C_f is the bed friction coefficient, D is the body dimension and H is the water depth.

The *Froude number* also characterizes the shallow water flow as it is another important parameter in free surface flows. It is defined as:

$$Fr = \frac{U}{\sqrt{g \cdot H}} \tag{2.3}$$

where U is the water velocity, g is the gravity and H is the water depth.

The Froude number indicates the relationship between the gravitational forces (as free surface perturbances) and inertial forces (as the flow velocity). As it is smaller, the gravitational forces are more important than the inertial ones. If the Froude number is greater than the unit means that the flow is supercritical and the information only travels downstream.

The influence of the shallow wake parameter on the flow behaviour depends on its relationship with the Reynolds number. As studied by Chen and Jirka [8], when the Reynolds number, referred to the water depth ($Re_h = U \cdot H/\nu$), is low ($Re_h < 1000$) the flow is dominated by the Reynolds number, without a relevant influence of the bottom surface friction. The viscous forces dominates over the inertial forces. On the other hand, when the Reynolds number is larger than 1500, then the flow is mainly influenced by the shallow wake paramenter (S).

Studies made by Monkewitz in [9] demonstrated that depending on the Reynolds number (Re) and on the velocity deficit, the wake behind a cylinder can exhibit *absolute instabilities* (with temporal growth rates), *convective instabilities* (with spatial growth) or be a *fully stable* flow.

The presence of bounding walls (bed and free surface) in shallow plane wakes has two separates effects that affect the wake behaviour:

a. **Kinematically**.

   The limited third dimension (water depth) prevents the three-dimensional breakdown of the regular vortex street flow. For that reason, the domain of a distinct von Karman vortex street pattern can be extended to Reynolds numbers vastly higher than for the unbounded wake. The three-dimensional vortex stretching process is absent for the large eddies whose size exceeds the flow depth and that have vertical alignment. Thus, the turbulent transfer process in low wavenumber range takes on the characteristics of two-dimensional turbulence with an *inverse energy cascade.*

b. **Dynamically**.

   The turbulence due to bottom surface friction will tend to suppress the transverse growth of disturbances that are part of the vortex street pattern.

Thus, the shallow water flow problems can be modelled as quasi-2D flow although in itself it is a 3D flow. The possibility to study this flow as 2D instead of 3D depends on the ratio between the vertical and the horizontal length scales.

$$\frac{H_n}{L_n} << 1 \qquad\qquad \frac{W_n}{U_n} << 1 \tag{2.4}$$

where U_n is the horizontal velocity rate, W_n is the vertical velocity scale, L_n is the horizontal length scale and H_n is the vertical length scale.

2.2 Turbulence models in SWE

2.2.1 Depth averaged Shallow Water Equations (SWEs)

In shallow water flow the RANS equations can be simplified to the depth averaged shallow water equations. The SWEs are depth averaged equations, and the flow is considered quasi-2D, giving three equations to solve:

$$\frac{\partial h}{\partial t}+\frac{\partial hU_j}{\partial x_j}=0 \tag{2.5}$$

$$\frac{\partial hU_i}{\partial t}+\frac{\partial hU_iU_j}{\partial x_j}=-gh(\frac{\partial h}{\partial x_i}+\frac{\partial z_b}{\partial x_i})-\frac{\tau_{b,i}}{\rho}+\frac{\partial}{\partial x_j}(\nu h\frac{\partial U_i}{\partial x_j})-\frac{\partial h\overline{u'_iu'_j}}{\partial x_j}$$

where U_i (i=1,2) are the two components of the depth-averaged velocity.

The fact that the SWEs solves the momentum equations in two directions instead of three reduces the computational cost notably.

2.2.2 k-ε model of Rastogi and Rodi

This model is applied for shallow water flows. It is applied to model the Reynolds stresses in the previous SWEs, solving the depth averaged value of the turbulent kinetic energy and dissipation. The transport equations are:

$$\frac{\partial kh}{\partial t}+\frac{\partial U_jhk}{\partial x_j}=\frac{\partial}{\partial x_j}\left[\left(\nu+\frac{\nu_t}{\sigma_k}\right)h\frac{\partial k}{\partial x_j}\right]+hP_k+hP_{kv}-h\varepsilon \tag{2.6}$$

$$\frac{\partial \varepsilon h}{\partial t}+\frac{\partial U_jh\varepsilon}{\partial x_j}=\frac{\partial}{\partial x_j}\left[\left(\nu+\frac{\nu_t}{\sigma_\varepsilon}\right)h\frac{\partial \varepsilon}{\partial x_j}\right]+hC_{\varepsilon_1}P_k\frac{\varepsilon}{k}+hP_{\varepsilon v}-hC_{\varepsilon_2}\frac{\varepsilon^2}{k} \tag{2.7}$$

$$P_{kv}=c_k\frac{u_f^3}{h} \qquad c_k=\frac{1}{c_f^{1/2}}$$

$$P_{\varepsilon v}=c_\varepsilon\frac{u_f^4}{h^2} \qquad c_\varepsilon=3.6\frac{c_{2\varepsilon}c_\mu^{1/2}}{c_f^{3/4}}$$

where C_f is the bed friction coefficient. The constants of the model are the same than the standard $k-\varepsilon$ model. Notice that the production terms are influenced by the bed friction, meaning that the turbulent kinetic energy has a component produced by bottom friction.

2.2.3 PANS equations applied to SWE

The equations of the PANS models are presented. The equations used are analogous to the $k-\varepsilon$ model but applying the filtering. Eq. 2.8 and 2.9 are the transport equations of the turbulent kinetic energy and the dissipation respectively.

$$\frac{\partial k_u h}{\partial t} + \frac{\partial U_j h k_u}{\partial x_j} = \frac{\partial}{\partial x_j}\left[\left(\nu_u + \frac{\nu_t}{\sigma_{ku}}\right) h \frac{\partial k_u}{\partial x_j}\right] + hP_u + hP_{kv} - h\varepsilon_u \tag{2.8}$$

$$\begin{aligned} \frac{\partial \varepsilon_u h}{\partial t} + \frac{\partial U_j h \varepsilon_u}{\partial x_j} = \frac{\partial}{\partial x_j}\left[\left(\nu_u + \frac{\nu_t}{\sigma_{\varepsilon u}}\right) h \frac{\partial \varepsilon_u}{\partial x_j}\right] &+ hC_{\varepsilon_1} P_u \frac{\varepsilon_u}{k_u} \\ &+ hP_{\varepsilon v} - hC_{\varepsilon_2} \frac{\varepsilon_u^2}{k_u} \end{aligned} \tag{2.9}$$

The variables k_u, ε_u, ν_u, σ_{ku}, $\sigma_{\varepsilon u}$ and P_u are defined in section 1.4.2.

Chapter 3

3 Experimental validation

In the experimental validation and in Chapters 4 and 5, all the simulations made in this work are 2D simulations. Li et.al in [17] compared several cases from Chen and Jirka ([8]) in 2D and 3D and conclude that 2D models are more accurate for low shallow wake parameters and 3D simulations are more accurate for high shallow wake parameters.

3.1 Free surface flow around a cylinder

Vortex shedding evolution

The flow field around a circular cylinder is primarily characterized by the creation of a symmetrical recirculation zone in the near wake. The recirculation zone contains a pair of stationary primary eddies of equal strength and opposite rotation. The behaviour of the recirculation zone can be explained referring to the dimensionless elapsed time:

$$t^* = \frac{t \cdot U}{D}$$

where t is the real time, U is the flow velocity and D is the characteristic dimension (the diameter in case of the circular cilinder). According to Chen and Jirka [8] in case of shallow water flow with an $S \leq 0.2$ and $Re_h \geq 1500$, the flow should present Von Kármán street. The evolution of the first instabilities downstream is explained with reference to t^* [10].

A similar analysis as in [10] is considered here, with a cylinder diameter of 0.32m, a water velocity of 0.22 m/s, a water depth of 2.5cm and a bed friction coefficient parameter of 0.0067. From this data, the real time can be calculated as: $t = t^* \cdot 1.88$.

First, at t^*=1 (Fig. 3.1(a)) the instabilities start to form behind the cylinder. As time advances (t^*=2), the instabilities keep growing and they begin to show a recirculation zone more clearly, as shown in Fig. 3.1(b). At t^*=3, the circular cylinder's recirculation zone experiences the largest reverse flow (Fig. 3.1(c)). These two vortices are the most energetic ones. After these two vortices are shed, the following vortices have less time to develop behind the cylinder,

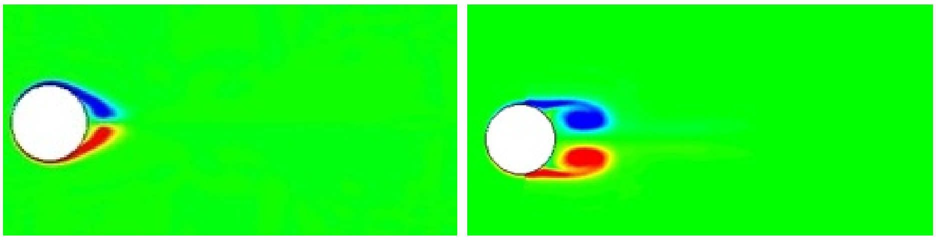

(a) t^*=1. Beginning of instabilities. (b) t^*=2. Developing of first vortices.

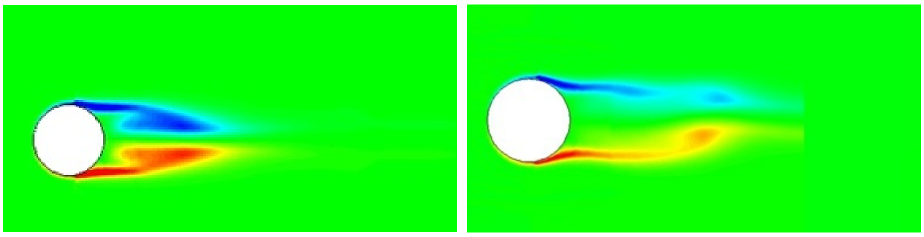

(c) t^*=3. Largest recirculation zones. (d) t^*=4. The primary eddies are shed.

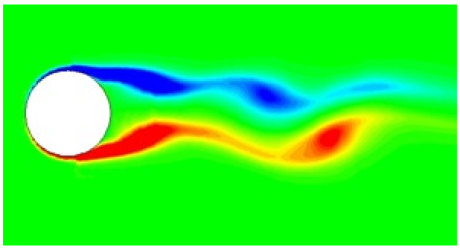

(e) t^*=5. Asymmetric flow. The primary eddies are shed.

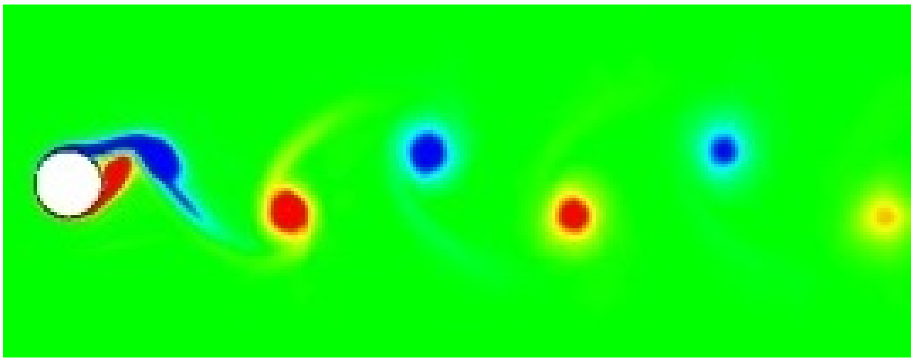

(f) t^*=6. Von Karman street

Figure 3.1: Vortex shedding around a circular cylinder

meaning that they cannot reach the same energy as the two first.

At t^*=4, the recirculation becomes asymmetric and the primary eddies are shed (Fig. 3.1(d)). The flow pattern has already changed from a symmetric flow to an asymmetric flow with vortex shedding. At t^*=5, the primary eddies are already shed and the next two asymmetric eddies begin also to be shed (Fig. 3.1(e)).

As mentioned before, the flow shows a Von Kármán vortex street when the vortex shedding becomes periodic (Fig. 3.1(f)). In this situation, the vortices are well-defined and they are shed with a certain frequency *f*. Regarding this frequency, the *Strouhal number* is a parameter that characterizes the flow and it defined as:

$$St = \frac{f \cdot D}{U} \tag{3.1}$$

The *Strouhal number* in a flow across a circular cylinder in incompressible flow approaches 0.2, but it can vary up to 0.18 or 0.22.

Lift coefficient

The area considered in the lift and drag coefficients (Eq. 1.8) in a cylinder case is calculated as: $A= D \cdot h$, where D is the diameter and h is the mean water depth. Fig. 3.2 shows the variation of the Lift Coefficient (C_L) in the previous flow around a circular cylinder with vortex shedding.

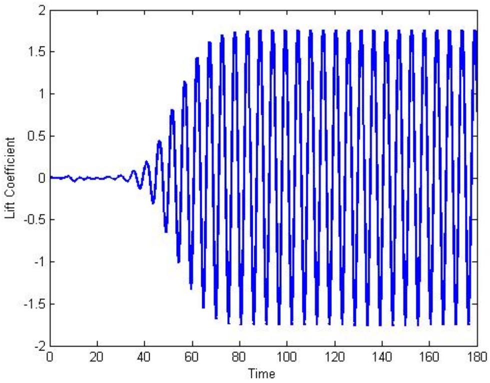

Figure 3.2: Lift coefficient in a regular circular cylinder case

At the beginning, the C_L starts to oscillate very slowly with a very small amplitude. At this time, the first two vortices are been built and then they shed. Until the Von Kármán street is achieved, and the flow is stabilized, the C_L has a progresive amplitude increase. Once the vortex street has a uniform shedding frequency, the C_L oscillation is periodic. This coefficient is supposed to have a mean equal to zero, indicating that the pairs of vortices are always symmetric and with equal energy.

Drag coefficient

In the flow over a cylinder into a open channel, the drag consists of three components:

a. **Surface drag**. Due to the shear stress acting on the cylinder surface.

b. **Form drag**. Due to the difference between the higher pressure on the upstream side of the cylinder, where the flow impacts and the water depth is greater, and the lower pressure in the wake or separation zone on the downstream side of the cylinder.

c. **Wave drag**. Due to the force required to form the standing surface waves around a cylinder.

In incompressible flow the drag coefficient varies with the Reynolds number, see Fig.3.3. However, in shallow water flow, this coefficient varies with the Froude number (Fr) (see Fig. 3.4), with the Reynolds number (Re) (see Fig. 3.5) and with the shallow water parameter (S).

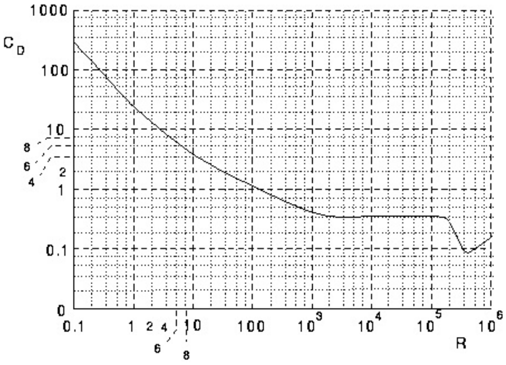

Figure 3.3: Drag coefficient variation with Reynolds number in incompressible flow, from [16]

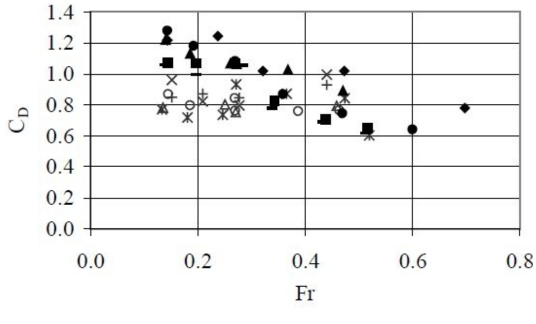

Figure 3.4: Drag coefficient variation with Froude number, from [15]

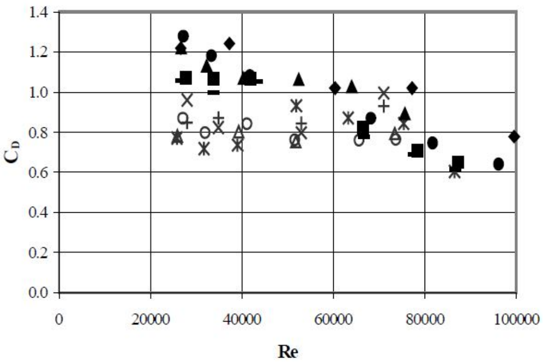

Figure 3.5: Drag coefficient variation with Reynolds number, from [15]

Analogous to the lift coefficient, in Fig. 3.6 the time-variation of the drag coefficient is shown. This coefficient starts to oscillate influenced on the creation of the first two vortices. At the beginning, the drag coefficient reaches its highest value, which is much larger that the mean drag value in the stable period. After this peak value, the drag coefficient diminish its value below 1 and grows until the uniform vortex street is formed. From this moment, the C_D oscillates periodically, with a frequency which is the double of the lift coefficient one.

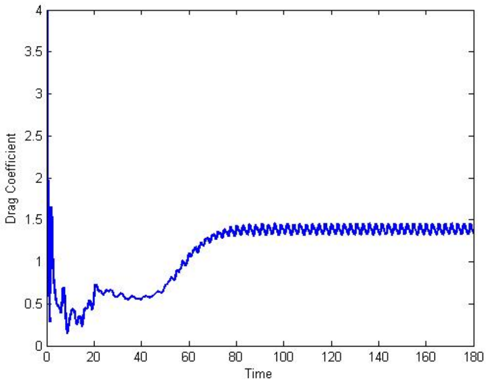

Figure 3.6: Drag coefficient in a regular circular cylinder case

3.2 Numerical vs experimental results

In order to validate the models used in this study, experimental data is needed to verify the computational analysis. For this propouse, the data from the study made by Chen and Jirka [8] was chosen. In this study, the free surface shallow water flow around a circular cylinder and a solid plate were analyzed in multiple situations where the water velocity (U), the water surface elevation (WSE) and the bluff body dimension (D) (diameter of the cylinder or length of the plate) were varied. The circular cylinder and the flat plate are the simplest problems concerning flow across bluff bodies, so it is a good way to analyze how accurate the computational approach is.

The cases chosen from the document [8] are the ones that were considered most interesting, regarding the relationship between the ambient Reynolds number (Re_h) and the wake shallow parameter (S). The type of instability pattern that appears downstream the bluff body depends on this relationship, which is different for each kind of bluff body. The three patterns are:

a. **Vortex Street (VS)**.

It is characterized by an oscillating vortex shedding mechanism. The fluid flow past the object creates alternating low-pressure vortices on the downstream side of the object. Fig. 3.7 shows a comparison between a real Vortex Street pattern and a VS calculated with our model. A VS has vortices that are shed uniformily (Von Kármán vortex street). The shedding frequency is constant over time.

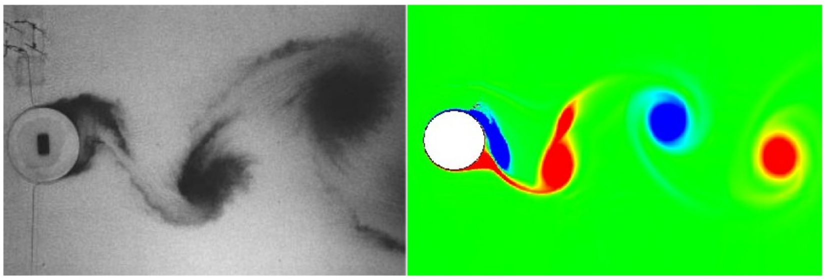

Figure 3.7: Vortex Street caused by a circular cylinder [8] and vorticity from our simulation (right)

b. **Unstable Bubble (UB)**.

Wake type with flow instabilities growing downstream of a recirculating bubble attached to the body. It takes place with a wake shallow parameter (S) larger than in the *VS* case. Fig. 3.8 shows this instability from [8] in a cylinder case, and the results from a solid plate got from our simulation. As a difference from VS, the vortices are not shed uniformly because the turbulence is higher and the flow is more chaotic.

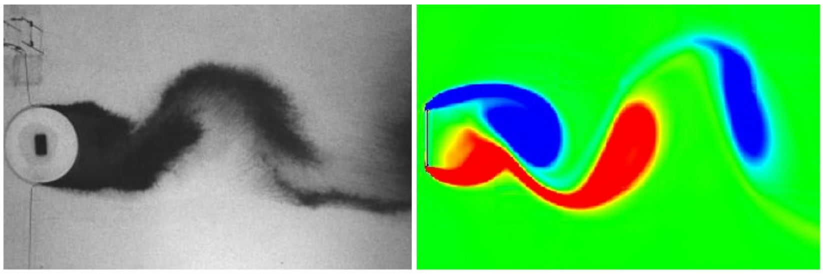

Figure 3.8: Unsteady Bubble in real water flow across a circular cylinder (left, from [8]) and vorticity from our simulation (right)

c. **Stable Bubble (SB)**.

Wake type with an attached bubble followed by a turbulent wake that contains no growing instabilities. In Fig. 3.9 another comparison is made between Chen and Jirka results and our CFD simulation.

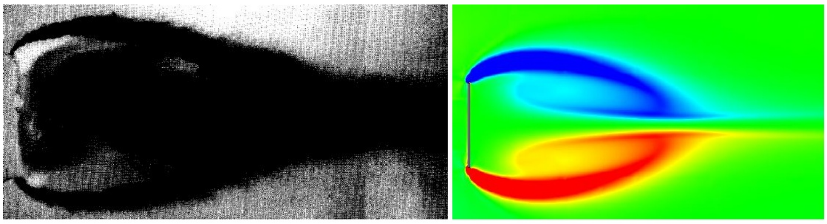

Figure 3.9: Steady Bubble in real water flow across a flat plate (left, from [8]) and vorticity from our simulation (right)

3.3 Classification diagrams

Chen and Jirka [8] made a classification diagram regarding the patterns found in the circular cylinder and in the flat plate. They found that the type of stability parameter S determines the downstream instability. There are two critical values of S that might be mentioned, because they correspond to the transition from one to another pattern. The first one corresponds to the transition from VS to UB. This one is named *convective-absolute instability*, S_{ac}. The second one is the *convective-convective instability*, S_{cc}, and corresponds to the UB transition to SB. According to [8], those values are shown in Table 3.3.

The fact that the SP case has lower S values is because its surface is completely perpendicular to the water flow direction, so the impact on the water flow is harder than in the CY, where the fluid flow has a smoother transition across the blunt body. These values are from the diagrams made by Chen and

	Circular cylinder (CY)	Solid plate (SP)
S_{ca}	0.20	0.16
S_{cc}	0.50	0.40

Table 3.1: Critical S values from [8]

Jirka in [8]. These are presented and discussed in the next section.

Chen and Jirka stablished that with a $Re_h \leq 1500$ the laminarity of the flow is dominant and the instabilities tend to be stabilized. The pattern shown in that case is stable bubble. This section study these diagrams and compare them with the results from our simulations.

Fig. 3.10 shows the diagram corresponding to the circular cylinder made by Chen an Jirka ([8]).

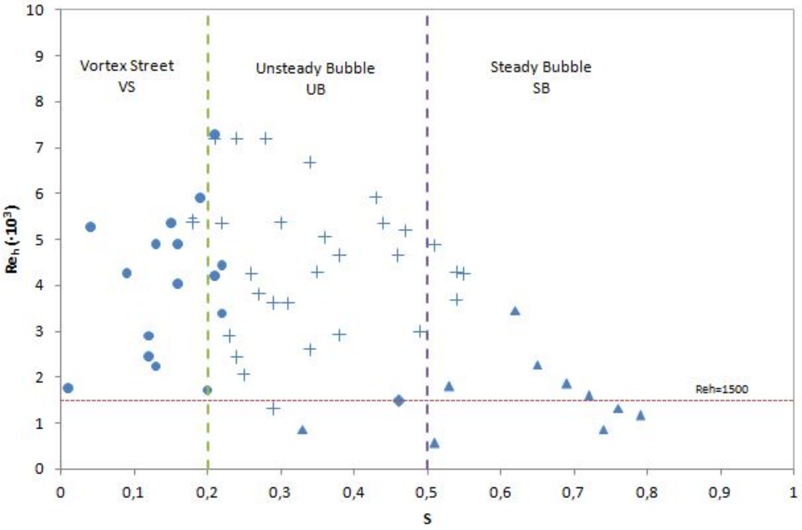

Figure 3.10: Classification diagram for the Circular Cylinder case. The • indicates Vortex Shedding, the + are the Unstable Bubble and △ are the Steady Bubble

The divisions proposed by Chen and Jirka fulfil almost all the cases. But if a more accurate division is sought, there are two points where to look at. First of all, some VS are placed in the left boundary of the UB region; and analogous some UB cases are placed in the SB region. This might mean that the critical S_{ca} is not constant with the Reynolds number. For the S_{cc} the situation is similar. The classification of Chen and Jirka indicates that there are two regions where there is a gradual transition from SB to UB and from UB to VS, and where more variables are needed to indicate the proper pattern.

The solid plate diagram shown in Fig. 3.11 has the same problems as the CY case, but more complex. In the SP case within the transition from VS to UB some cases are mixed and there is no a clear division. Again, a gradual transition from one pattern to another the UB pattern with a small recirculation zone (Fig. 3.8) is really close to a VS status. In this study these regions are analyzed in deep to determine some reasons why these transition zone behaviours happens.

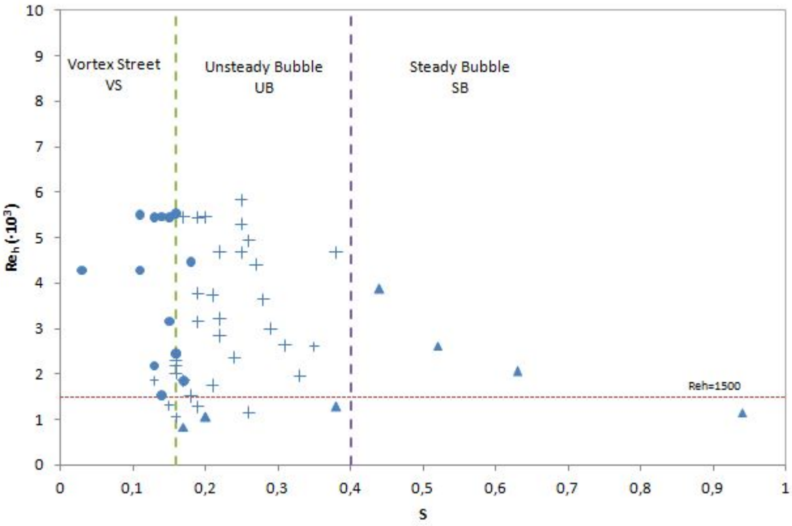

Figure 3.11: Classification diagram for the Solid Plate case. The symbols represents the same than in Fig. 3.10

3.4 Physical Scenario

As in every Computational Fluid Dynamics problem, the mesh and bluff bodies design are the first step in the problem analysis. As explained in the second chapter, the shallow water flows can be considered two-dimensional as the vertical acceleration can be neglected. Thus, the computational analysis will be done in two dimensions. Figures 3.12(a) and 3.12(b) show the circular cylinder and the solid plate used in our simulations.

The domain where the water flows is a rectangular tank that measures 780cm length and 600cm width. With this data and the dimensions of the cylinder and

(a) Circular cylinder

(b) Circular cylinder

Figure 3.12: Used bluff bodies. D indicates the main dimension.

plate, the meshes were designed. Three meshes were used for each circular cylinder and flat plate, depending on the body length (D). The next figures show one of the mesh used in the circular cylinder (Fig. 3.13) case and one mesh used in the solid plate (Fig. 3.14) case. Concerning the turbulence model, in this chapter *URANS* with the depth-averaged $k-\varepsilon$ model of Rastogi and Rodi was used, meanwhile other turbulence models as PANS and filter-based URANS are used in following chapters.

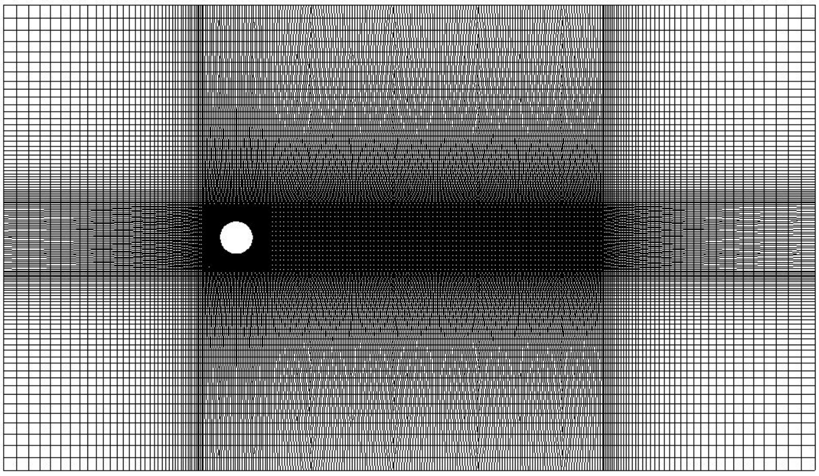

Figure 3.13: Example of a mesh used in the circular cylinder case

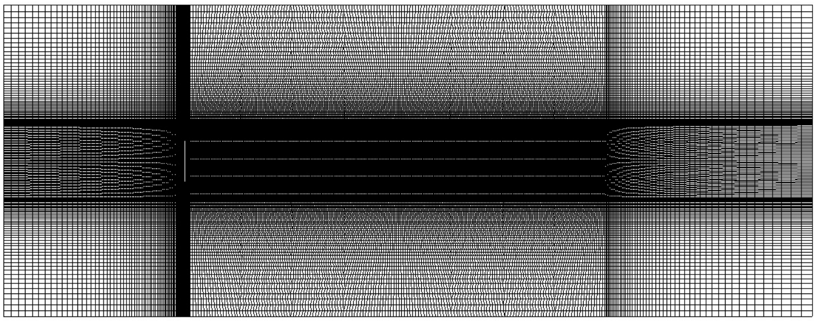

Figure 3.14: Example of a mesh used in the flat plate case

3.5 Simulation data and results

From the simulations in [8], there were chosen 17 cases from the CY (Table 3.2)and 19 from the SP (Table 3.3). These are mostly critical points, where it is not easy to differ from VS or UB. However, some of them are also well-defined cases but they were used to be sure that the computational model is good enough.

3.5.1 Numerical scheme

The code used in the simulations is *Turbillon* [6]. For the cases studied in this work the code requires the following input data to run the model.

- Inlet water flow, Q_{in} (m/s^2)
- Bottom friction coefficient *Cf*, ($\tau_b = \rho \cdot c_f \cdot U^2$).
- Outlet water elevation H_{out} (m).

Wall functions are used at the bluff body boundary. In this chapter, a standard numerical scheme is used to solve the shallow water equations.

3.5.2 Circular cylinder data and results

Table 3.2 shows all the CY cases which are modelled. Every case is named with the same reference from [8].

Name	U(m/s)	H_{mean}	D (m)	C_f	S	Re_h	Fr	Observed	CFD
CY3	0.170	0.025	0.32	0.0067	0.0858	4250	0.343	VS	VS
CY4	0.145	0.020	0.32	0.0074	0.1184	2900	0.327	VS	VS
CY5	0.123	0.020	0.32	0.0078	0.1248	2460	0.278	VS	VS
CY13	0.089	0.060	1.40	0.0063	0.1470	5340	0.116	VS	**SB**
CY15	0.029	0.060	1.40	0.0086	0.2007	1740	0.038	VS	**SB**
CY16	0.182	0.040	1.40	0.0059	0.2065	7280	0.291	VS	VS
CY17	0.145	0.020	0.62	0.0074	0.2294	2900	0.327	UB	UB
CY19	0.103	0.020	0.62	0.0082	0.2542	2060	0.233	UB	**SB**
CY23	0.066	0.020	0.62	0.0093	0.2883	1320	0.149	UB	**SB**
CY28	0.109	0.050	1.40	0.0063	0.1764	5450	0.156	UB	UB
CY35	0.267	0.025	1.40	0.0060	0.3360	6675	0.539	UB	UB
CY44	0.271	0.018	1.40	0.0065	0.5056	4878	0.645	UB	UB
CY46	0.245	0.018	1.40	0.0067	0.5211	4410	0.583	UB	UB
CY48	0.043	0.020	0.62	0.0106	0.3286	860	0.097	SB	SB
CY49	0.038	0.015	0.62	0.0122	0.5043	570	0.099	SB	SB
CY51	0.216	0.016	1.40	0.0071	0.6213	3456	0.545	SB	SB
CY54	0.094	0.017	1.40	0.0088	0.7247	1598	0.230	SB	SB

Table 3.2: Data used in circular cylinder case. The last two columns indicate the flow pattern observed in the experiments of Chen and Jirka [8] and in our numerical simulations.

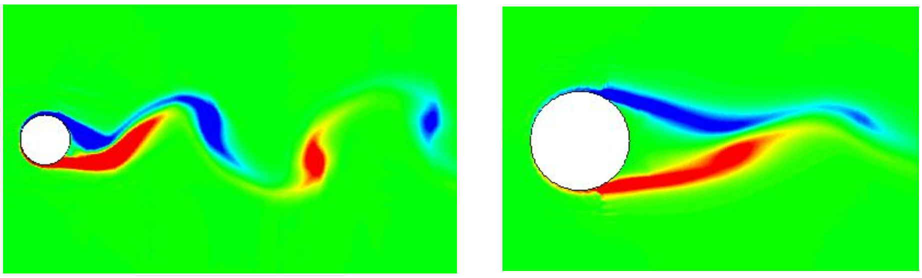

(a) CY 3. The vortices are simulated quite smooth

(b) CY 28. Unsteady bubble regular simulation

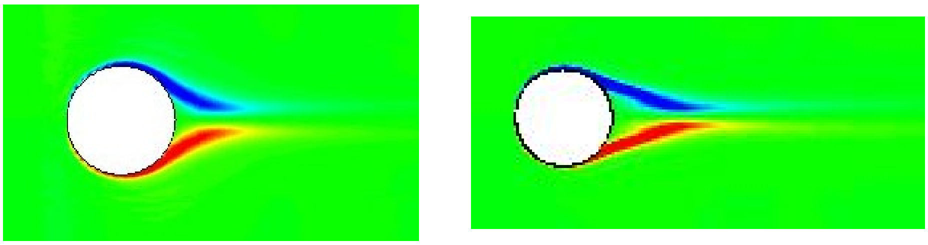

(c) CY 15. No vortex street is simulated.

(d) CY 23. No unsteady bubble is simulated.

Figure 3.15: Instability patterns in circular cylinder CFD simulations.

All these cases were simulated and the results were globally satisfactory. Only 4 cases (from 17) as CY 13, 15 (Fig. 3.15(c)), 19 and 23 do not show the corresponding pattern. The flow achieved does not show any instability downstream. Notice that the Froude number in these cases is really small.

The VS of the case CY 3 is shown in Fig. 3.15(a). An UB case is shown in Fig. 3.15(b), corresponding to the case CY 28. Notice that there is a recirculation zone downstream the cylinder, and the vortices are shed further downstream in a UB case than in a VS case. Both Figures 3.15(c) and 3.15(d) are problematic simulations, and not instability takes place. From Table 3.2 a possible reason for the non satisfactory cases is that the Froude number is quite low. All of the 4 problematic cases have a $\mathrm{Fr} \leq 0.25$. It seems that this model is not able to reproduce the unsteady oscillations when the Froude number is low. This is probably due to an excessive dissipation introduced by either the turbulence model and the numerical scheme.

3.5.3 Solid plate data and results

This section is analogous to the circular cylinder. The data from the 19 cases which were modelled is given Table 3.3.

The solid plate produces a more drastic change on the flow field, which is not as smooth as it is in the circular cylinder. This causes that the energy of the vortices is now greater than in the CY. The only issue, explained already in the SP diagram classification, is the fact to distinguish a VS and a UB where the recirculation zone is small. The VS case is represented in Fig. 3.16(a). The

Name	U(m/s)	H_{mean}	D (m)	C_f	S	Re_h	Fr	Observed	CFD
SP2	0.171	0.025	0.4	0.0067	0.107	4275	0.345	VS	VS
SP6	0.123	0.025	0.4	0.0078	0.125	3075	0.248	VS	VS
SP7	0.297	0.015	0.4	0.0066	0.176	4455	0.774	VS	VS
SP12	0.061	0.040	0.8	0.0078	0.156	2440	0.097	VS	VS
SP14	0.052	0.025	0.4	0.0093	0.149	1300	0.105	UB	UB
SP15	0.042	0.025	0.4	0.0100	0.160	1050	0.085	UB	UB
SP16	0.093	0.020	0.4	0.0084	0.168	1860	0.210	UB	UB
SP17	0.076	0.020	0.4	0.0089	0.178	1520	0.172	UB	UB
SP18	0.251	0.015	0.4	0.0069	0.184	2765	0.654	UB	UB
SP19	0.210	0.015	0.4	0.0073	0.195	3150	0.547	UB	UB
SP20	0.077	0.015	0.4	0.0069	0.259	1155	0.201	UB	UB
SP21	0.047	0.040	0.6	0.0084	0.126	1880	0.075	UB	UB
SP22	0.272	0.020	0.6	0.0063	0.189	5440	0.614	UB	UB
SP25	0.161	0.020	0.6	0.0072	0.216	3220	0.363	UB	UB
SP28	0.200	0.013	0.6	0.0077	0.355	2600	0.560	UB	UB
SP33	0.182	0.030	0.8	0.0063	0.168	5460	0.335	UB	UB
SP35	0.218	0.025	0.8	0.0063	0.202	5450	0.440	UB	UB
SP47	0.033	0.025	0.4	0.0107	0.171	825	0.067	SB	SB
SP50	0.064	0.020	0.8	0.0094	0.376	1280	0.144	SB	SB

Table 3.3: Data used in Solid Plate case.

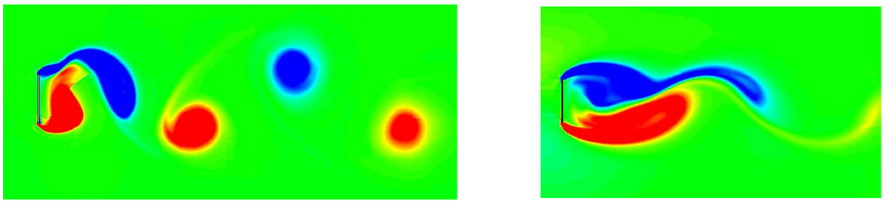

(a) SP 12. Vortex shedding

(b) SP 28. Unsteady bubble

Figure 3.16: Instability patterns in solid plate CFD simulations.

SP 28 belongs to the UB cases, it is represented in Fig. 3.16(b).

Table 3.3 show the results from our simulations. All cases in CFD reproduce the observed pattern in experimental analysis by Chen and Jirka. The instabilities produced downstream the flat plate have more energy than with the circular cylinder as the flow change is less smooth. The numerical scheme simulates better these more energetic instabilities giving a totally agreement between CFD and experimental results.

Chapter 4

4 Analysis of the numerical schemes used to solve the SWE

The accuracy of a CFD simulation depends on several factors as mesh refinement, the numerical scheme, the turbulence model or the time step. In this chapter, five different numerical schemes are used to solve the URANS equations. These numerical schemes are:

a. **HLL**. This scheme is very common for shallow water flows applications. It is very diffusive and therefore it presents problems to solve intermediates waves in vortical flows.

b. **HLLC**. It is an evolution from the HLL. It has less numerical diffusion than the HLL.

c. **HLLCC**. This scheme is an extension of HLLC, which disminishes its numerical diffusion.

d. **Roe**. This scheme along with the HLL and HLLC are the most common numerical schemes for the shallow water equations (SWEs), [7].

e. **Upwind-HLL**. This is an hybrid scheme between the HLL and a standard upwind scheme which is intended to be less diffusive than the HLL.

The HLL, HLLC and Roe schemes are quite diffusive and they are appropiate to solve rapidly varying flow where shock waves might develop. However, for some applications where the flow is always subcritical, numerical schemes with a less amount of numerical diffusion might be more appropiate, this are the cases of the HLLCC and the Upwind-HLL schemes.

The cases analyzed in this chapter were modelled with a standard depth-averaged $k-\varepsilon$ turbulence model and a time step of 0.05s. The mesh refinement is analyzed as well as the numerical scheme. The model input data is presented in Table 4.1, which approaches the CY3 case from Table 3.3.

Inlet velocity	Cylinder Diameter	S	Re_h	Fr	Cf
0.17 m/s	0.32m	0.0858	4250	0.343	0.0067

Table 4.1: Input data of the model in simulations.

4.1 Mesh convergence

The mesh size is very important in eddy resolving turbulence models like filter-based URANS or PANS.

Three different meshes have been analyzed. In order to compare the results, one numerical scheme had to be fixed, and in this case the used one was the HLLCC. Table 4.2 shows the number of elements and nodes in each mesh.

Refinement	Elements	Nodes
Coarse	33944	29883
Medium	55662	47242
Fine	85496	67129

Table 4.2: Elements and nodes of the used meshes.

Fig. 4.1 represents the coarse mesh used in the simulations. Both Fig. 4. 2(a) and 4.2(b) show the detailed mesh around the cylinder with the fine and coarse discretization respectively.

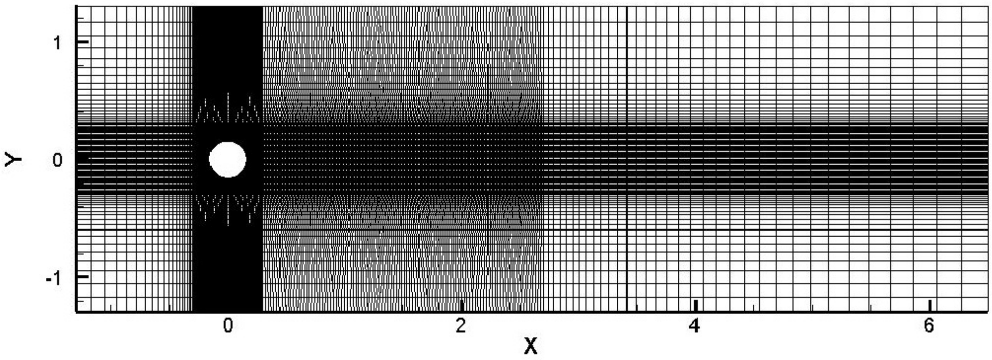

Figure 4.1: Coarse mesh.

In order to compare the results from the different meshes, they are got from a line perpendicular to the flow (Fig. 4.3) .Fig. 4.4 shows that the coarse mesh predicts a higher horizontal velocity at y=0m, where the lowest velocity value is reached. The fine and medium meshes have really close values. In Fig. 4.5 the dissipation does not show any relevant difference between the three meshes.

Regarding the resolved kinematic energy (Fig. 4.6), the coarse mesh has a

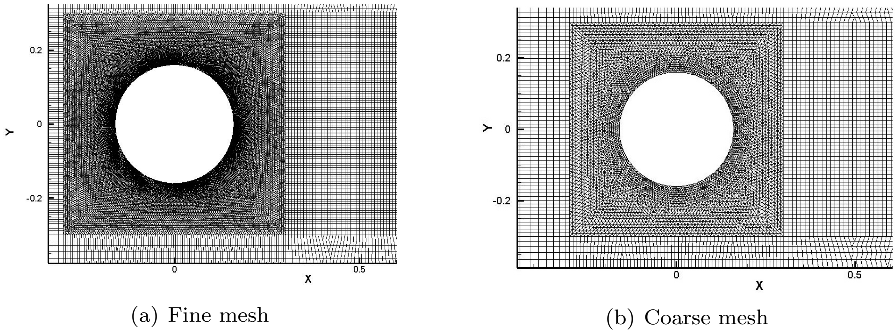

(a) Fine mesh (b) Coarse mesh

Figure 4.2: Detail of the mesh around the cylinder.

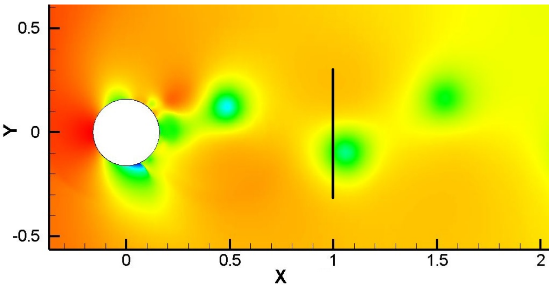

Figure 4.3: Location of the profile used for plotting variable profiles (water surface elevation plotted).

symmetric profile, but the values are quite lower compared to the fine mesh profile which is symmetric as well. The medium mesh does not look perfectly symmetric but its values are closer to the fine mesh.

Hence, the mesh convergence analysis indicates that the fine mesh has an appropiate resolution, and therefore, it was used in all the following simulations.

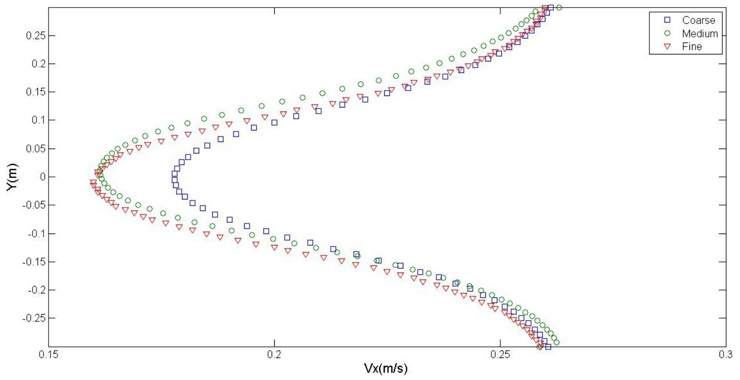

Figure 4.4: Horizontal velocity along a vertical profile at 1 meter downsteam the cylinder center.

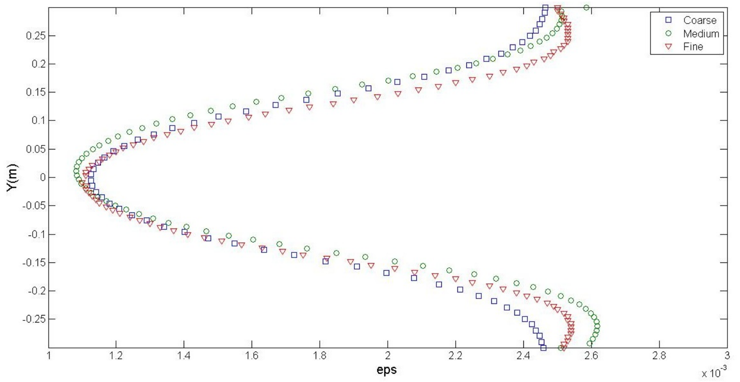

Figure 4.5: Dissipation along a vertical profile at 1 meter downsteam the cylinder center.

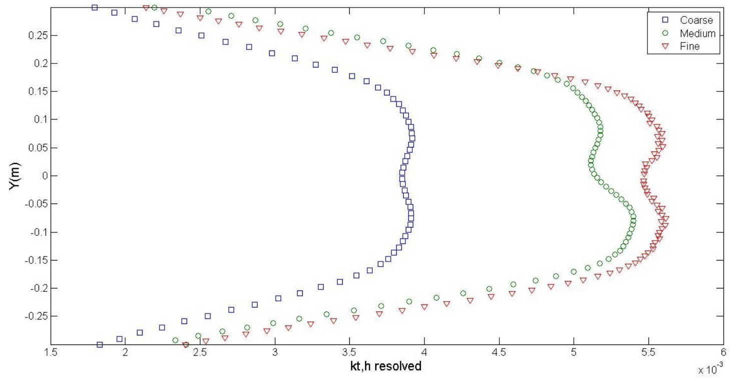

Figure 4.6: Resolved kinetic energy along a vertical profile at 1 meter downsteam the cylinder center.

4.2 Influence of the numerical scheme in the results

All the numerical schemes used have second order accurate in space, because first order schemes are very diffusive and damp the oscillations.

In the oscillations due to vortex shedding, the lift coefficient is supposed to have a mean value of zero. Therefore, its root mean square ($rms(C_L)$) is used to study each numerical scheme. On the other hand, the mean value of the drag coefficient ($\overline{C_d}$) in the stable periodic state is analyzed, and compared with experimental results, as in [15]. Table 4.3 summarizes the $rms(C_L)$ and $\overline{C_d}$ results from all the schemes with different order accurate in time. All the schemes do not show large differences with first and second order accurate in time but the HLLC where the first order has a very low $rms(C_L)$.

Scheme	Time order accurate	$\overline{C_d}$	$rms(C_L)$
HLL	1^{st} order	1.0734	1.0169
	2^{nd} order	1.0925	1.0413
HLLC	1^{st} order	0.7118	0.1926
	2^{nd} order	0.9899	1.2784
Roe	1^{st} order	1.3783	1.2267
	2^{nd} order	1.3786	1.2272
HLLCC	1^{st} order	1.6236	1.3471
	2^{nd} order	1.6245	1.3412
Upwind-HLL	1^{st} order	1.7445	1.4480
	2^{nd} order	1.7167	1.4264

Table 4.3: Comparison of the numerical schemes with different time order accurate results.

To provide an easier comparison, some of the lift (Fig. 4.8) and drag (Fig.4.7) coefficienst are plotted. Some reference points about the results might be mentioned:

- The schemes HLL and HLLC give mean drag results close to 1, what is lower than other methods. This means that the drag produced by the vortex creation due to suction is smaller.

- The schemes HLLCC and Upwind-HLL (Fig. 4.7) achieve drag coefficient results a bit higher than the maximum value achieved in [15], which is close to 1.4 (see Fig. 3.4).

- The standard Roe method offers a coherent drag coefficient, approaching 1.4. As it is going to be shown, the lift and drag coefficient with this numerical scheme is uniformly periodic. This is the reason why its $rms(C_l)$ is lower than for the HLLCC and Upwind-HLL, with a larger irregularity in the coefficients behaviour.

In the following, Roe, HLLCC and Upwind-HLL are discussed.

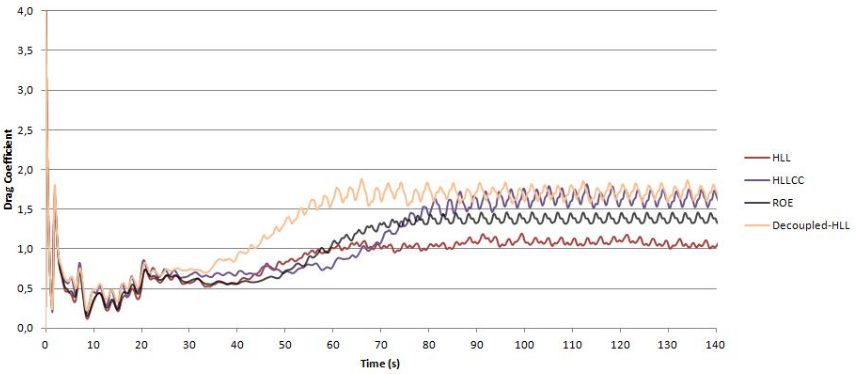

Figure 4.7: Drag coefficient scheme comparison.

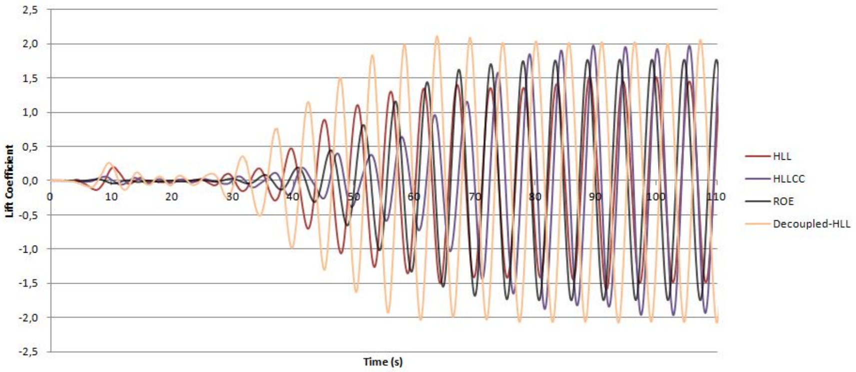

Figure 4.8: Lift coefficient scheme comparison.

4.2.1 Total kinetic energy

The differences between Roe, HLLCC and Upwind-HLL schemes are present in the instantaneous total kinetic energy plots, which is the sum of the resolved and modelled kinetic energy terms. Roe scheme (see Fig. 4.9(a)) solves lower kinetic energy than the other two (Fig. 4.9(b) and Fig. 4.9(c)) because it is more diffusive. Downstream the cylinder, the red color indicates the higher kinetic energy, and its area is smaller in the Roe scheme.

Fig. 4.10(a), 4. 10(b) and 4.10(c), show the average value of modelled kinetic energy in the whole domain along 100s when the flow is stable. Comparing the cylinder surrounds, with the Roe scheme the resolved kinetic energy is lower than with HLLCC or Upwind-HLL.

In order to compare the values of the modelled and resolved turbulent kinetic energies, a good approach is to integrate this values in the whole domain. This is shown in Table 4.4.

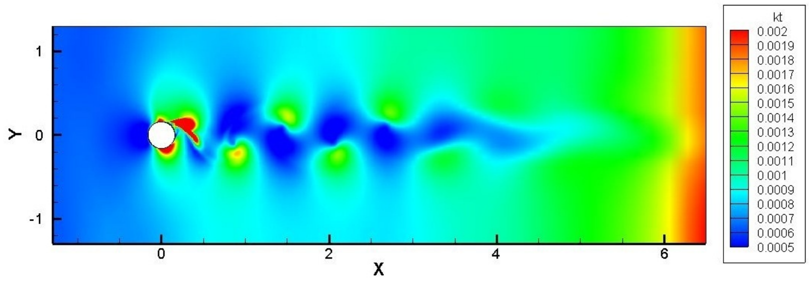

(a) Roe scheme.

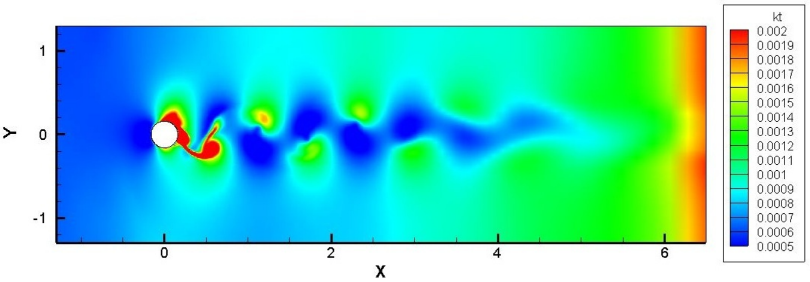

(b) HLLCC scheme.

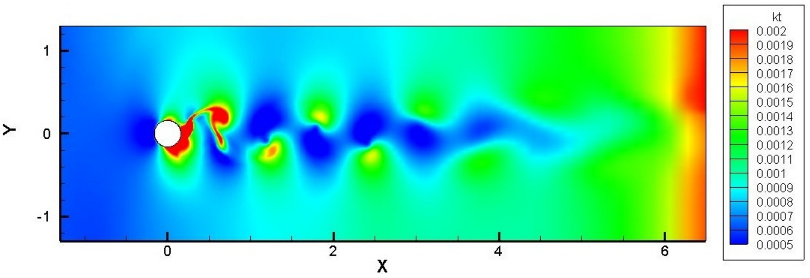

(c) Upwind-HLL scheme.

Figure 4.9: Instanteneous total kinetic energy.

The resolved kinetic energy averaged over 100 seconds for Roe, HLLCC and Upwind-HLL are shown in Fig. 4.11(a), 4.11(b) and 4.11(c). The largest differences are obtained just downstream the cylinder, where the vortex cores are created and shed.

Scheme	Total modelled kinetic energy	Total resolved kinetic energy
Roe	$1.9726 \cdot 10^{-2}$	$1.1197 \cdot 10^{-2}$
HLLCC	$2.0025 \cdot 10^{-2}$	$1.5344 \cdot 10^{-2}$
Upwind-HLL	$2.0229 \cdot 10^{-2}$	$1.6414 \cdot 10^{-2}$

Table 4.4: Comparison of the average total modelled and resolved kinetic energy values (m^2/s^2).

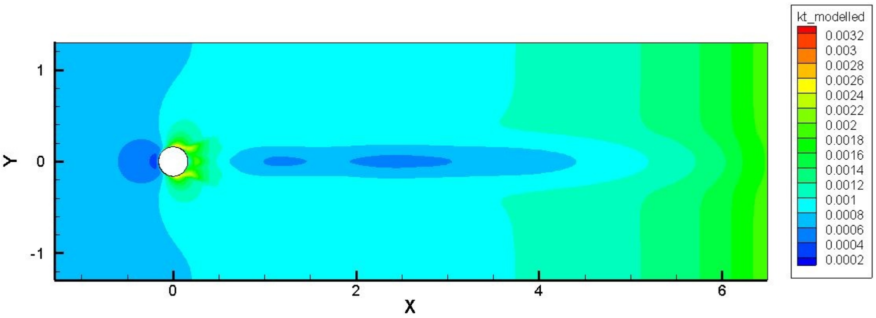

(a) Roe scheme.

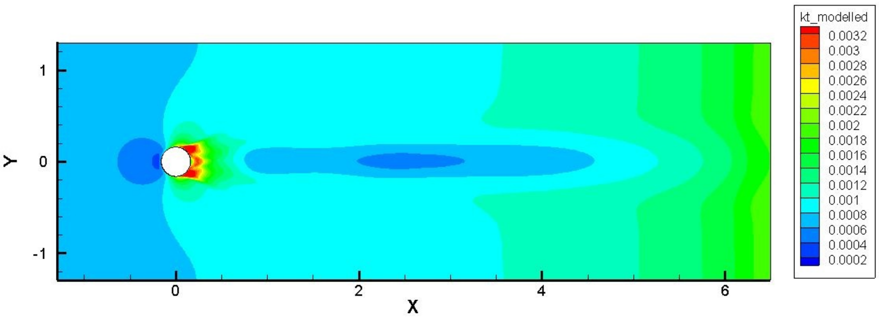

(b) HLLCC scheme.

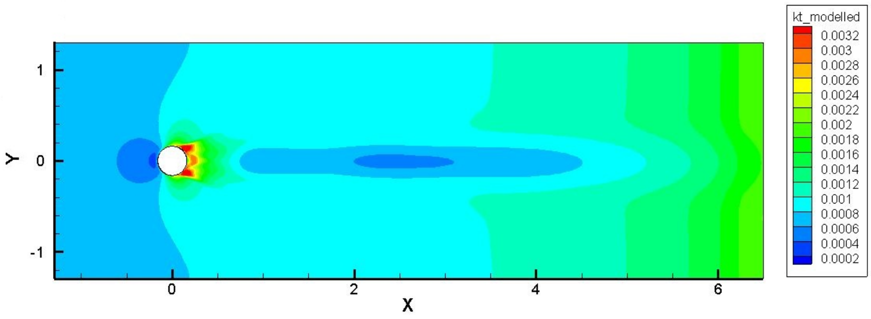

(c) Upwind-HLL scheme.

Figure 4.10: Average field values of modelled kinetic energy since the vortex shedding is uniform, during 100s.

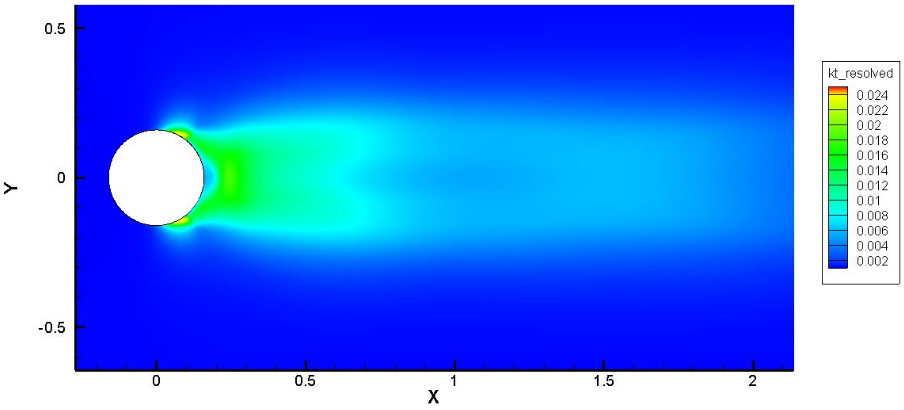

(a) Roe scheme.

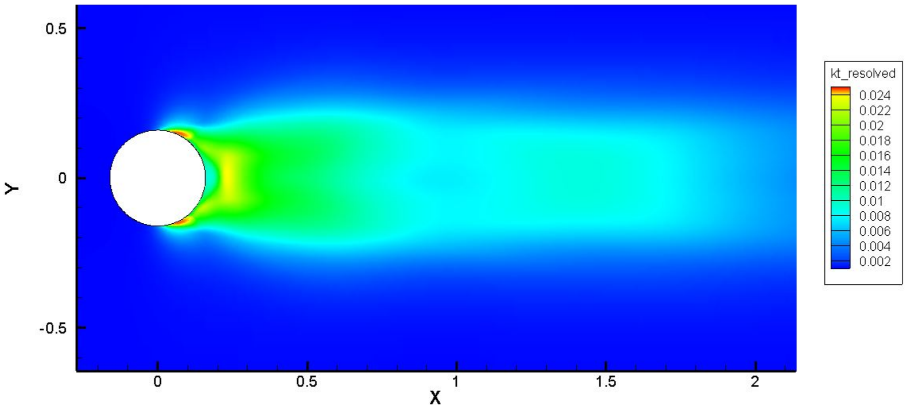

(b) HLLCC scheme.

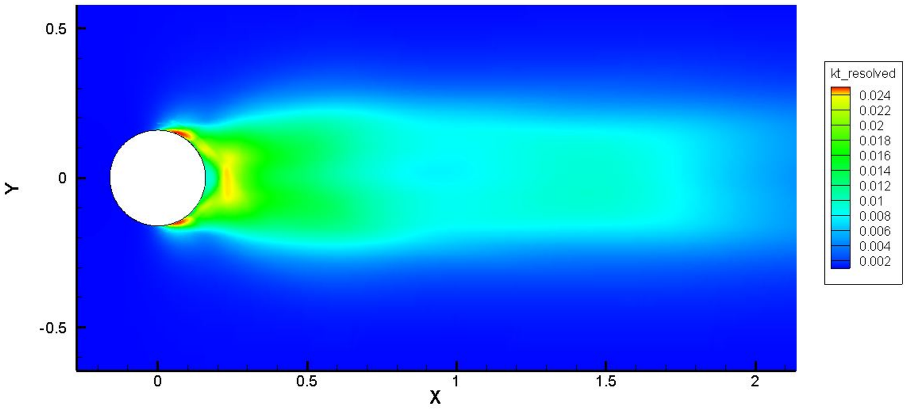

(c) Upwind-HLL scheme.

Figure 4.11: Average field values of resolved kinetic energy since the vortex shedding is uniform, during 100s.

4.2.2 Energy spectrum comparison

Fig. 4.13 represents the energy spectrum extracted from a point within the domain, presented in Fig. 4.12. The area under the spectrum gives the energy that the scheme solves. Roe scheme gives lower results as it is the most diffusive scheme of these 3. Fig. 4.13 represents the energy-frequency spectrum computed from the horizontal velocity in a fixed point during 100s. The second largest energy peak has a frequency around 0.18-0.19Hz in all the schemes.

The turbulent energy that each method resolves is shown in Table 4.5. The values are obtained integrating the kinetic turbulent energy along the whole frequencies range.

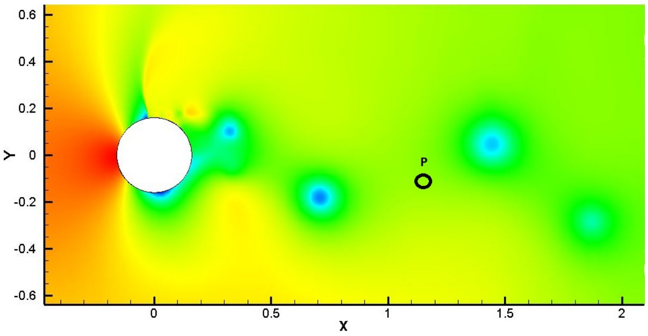

Figure 4.12: Point from where the spectrum data is got. Instantaneous water surface elevation plotted.

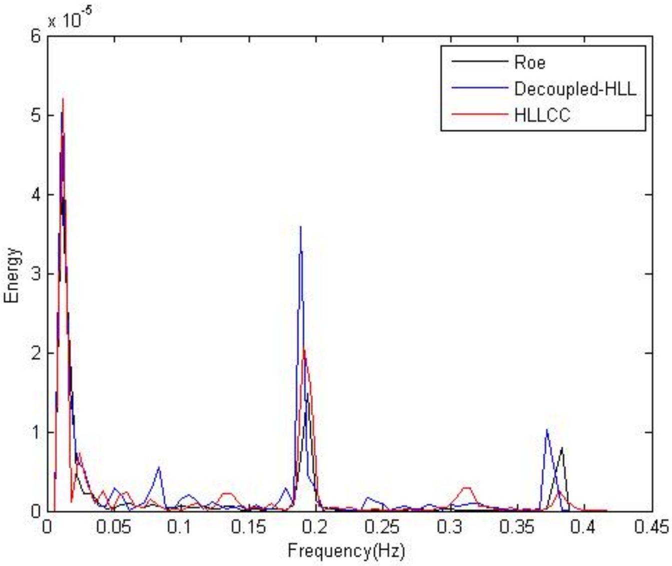

Figure 4.13: Energy spectrum comparison

Scheme	Energy quantity
Roe	0.0037
HLLCC	0.0044
Upwind-HLL	0.0045

Table 4.5: Comparison of the resolved turbulent kinetic energy.

As a result, it can been concluded that the three numerical schemes model the kinetic energy differently. The Upwind-HLL solves the largest amount of turbulent energy, as it is the less diffusive scheme. In Fig. 4.13, the Upwind-HLL solves secondary frequencies with higher energy than the other two schemes. The Upwind-HLL gives quite the same energy for the first and second peak frequencies and close to 4 times lower energy in the third. Roe scheme spectrum approaches more to the HLLCC spectrum but with lower energy values in each peak, as it is more diffusive.

Chapter 5

5 Turbulence modelling analysis

In the previous chapter, the influence of the numerical schemes in the results was studied. In this chapter, we analyze the influence of the turbulence modelling approach on the results. The numerical scheme used in the following simulations is the HLLCC, preventing a high numerical diffusion in the model. The simulations use the input data from Table 5.1:

Inlet velocity	Cylinder Diameter	S	Re_h	Fr	Cf
0.17 m/s	0.32m	0.0858	4250	0.343	0.0067

Table 5.1: Turbulence model simulation details.

5.1 Turbulence models

The turbulence models used in the simulations presented in this chapter are PANS, filter-based URANS (FB) and URANS. The aim of this chapter is to study how the filter size ($\triangle$) in filter-based URANS, or the unresolved-to-total kinetic energy ratio (f_k) in PANS, affects the turbulent kinetic energy, dissipation, velocity, etc. and to compare the results with URANS solutions. Note that the URANS model is the same as the PANS model with the f_k ratio equal to 1.

The PANS model defines the filtering factor as a function of the turbulent kinetic energy which we want to solve. On the other hand, the FB has a filter size related to the size of the eddies that we want to resolve. The applied filter is the lowest value of the vortices to be solved. In the FB analysis, the filter size is related to the water surface elevation (h = 0.025m) and to the mesh size (dx = 0.008m).

5.2 PANS

The PANS model have been analytically described with its equations in Chapter 2. The influence of the control parameters (f_k and f_ε) on the results are explained in the following. These control the relation between the total and the unresolved kinetic energy and dissipation. Thus, the amount of resolved turbulence is determined by these parameters. f_ε is always 1 [13] and thus f_k is the controlling parameter. Note that for cases with a reduced f_k a finer mesh is needed, as a requirement used for DNS simulations.

In terms of turbulent kinetic energy, f_k affects inversely to the modelled and to the resolved kinetic energy quantities:

a. Modelled kinetic energy: as this is the one given from the $k - \varepsilon$ equations, the lower f_k is, the lower the modelled kinetic energy is. Hence, the amount of modelled kinetic energy is lower as the f_k becames lower.

b. Resolved kinetic energy: the lower is the f_k the higher is the resolved turbulence. As f_k approaches 0, the results approach a DNS model, provided that the mesh is fine enough; and when f_k approaches 1, the model tends to a RANS simulation. Thus, the model *resolves* larger kinetic energy as f_k is lower.

The cases analyzed with PANS are presented in Table 5.2.

f_ε	f_k
1	1.0
1	0.8
1	0.6
1	0.4
1	0.2

Table 5.2: Cases simulated with PANS.

Vorticity

The vortices are the result of the shear forces that appear in the flow dowstream the cylinder. The resolved vorticity field will vary as the turbulence model changes. In this section, the vortices are compared between different PANS simulations.

The first point studied is the separation between vortex cores, what indicates how random is the vortex shedding (Fig. 5.1(a) to 5.1(e)). The hydrodynamic coefficients oscillate depending also on the uniformity of the vortex shedding. PANS with $f_k = 1.0$ presents an equidistant separation between the vortices and its lift coefficient oscillates uniformly (Fig. 5.2(a)). Fig. 5.3(a) represents the energy-frequency spectrum for this case.

The differences between PANS with $f_k = 1.0$ and 0.8 are not significant. Both lift coefficients (Fig. 5.2(b) and 5.2(a)) are very similar. However, the

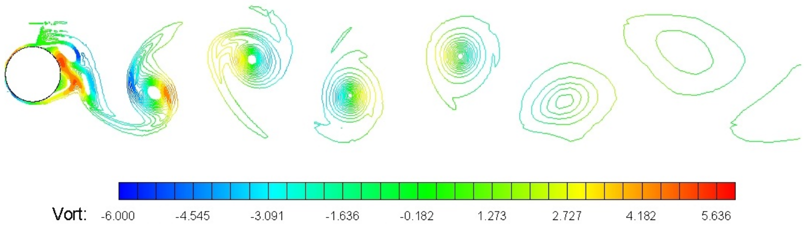

(a) PANS f_k = 1.0

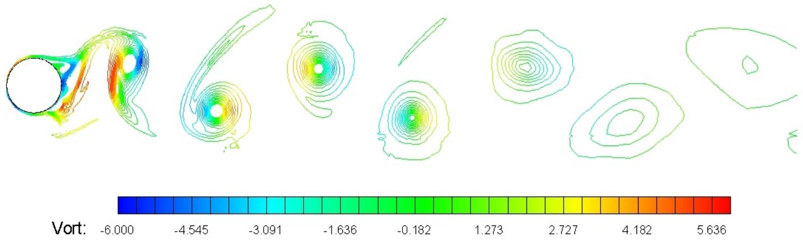

(b) PANS f_k = 0.8

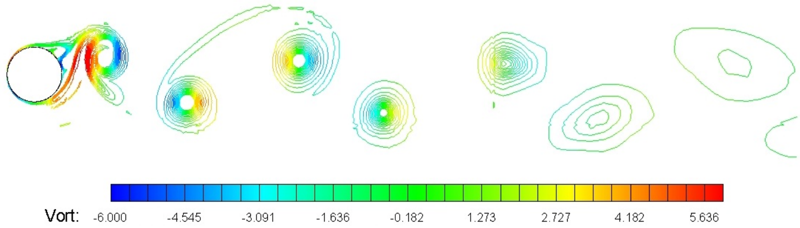

(c) PANS f_k = 0.6

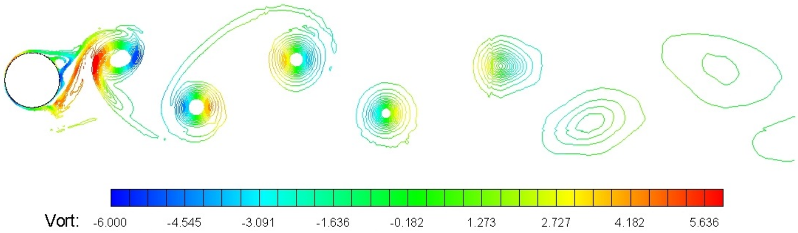

(d) PANS f_k = 0.4

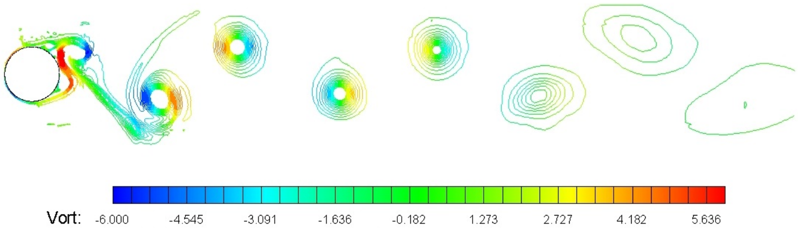

(e) PANS f_k = 0.2

Figure 5.1: Vorticity velocity contour lines at t= 160s (t*=110) in PANS simulations.

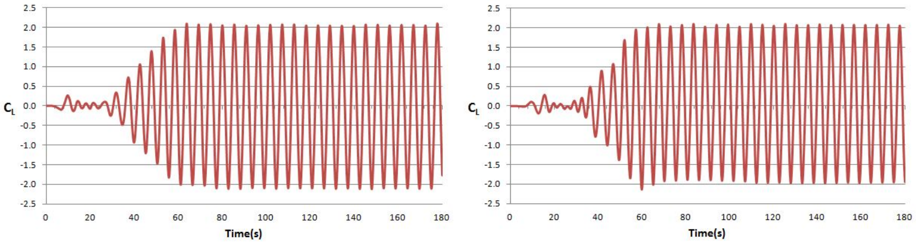

(a) PANS $f_k = 1.0$ (b) PANS $f_k = 0.8$

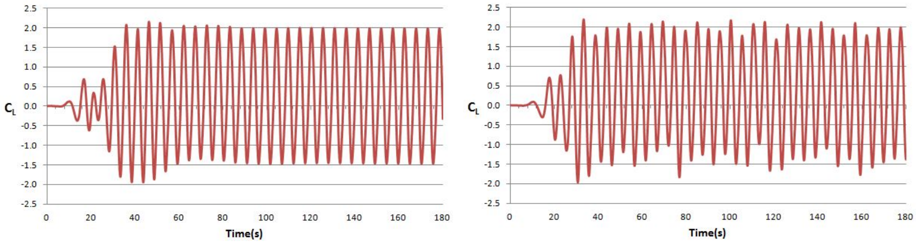

(c) PANS $f_k = 0.6$ (d) PANS $f_k = 0.4$

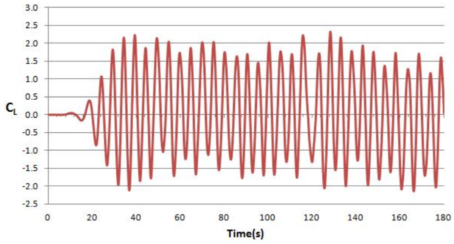

(e) PANS $f_k = 0.2$

Figure 5.2: Lift coefficient in PANS simulations.

spectrums associated to these models show that the energy associated to the frecuency 0.2Hz becames larger. On the contrary, in PANS with $f_k = 0.6$, 0.4 and 0.2, the distance between the vortex cores is not equal. It is in PANS simulations with $f_k = 0.4$ and 0.2 when the high turbulence is reflected in the lift coefficients (Fig. 5.2(d) and 5.2(e)) as the oscillation is not uniform. Meanwhile, for $f_k = 0.6$ the oscillation is uniform with a larger amplitude in the first part.

Energy spectrum

The effect of the instabilities is also reflected in the energy-frequency spectrum from a point placed at X=1.17m, Y=-0.1m (Fig. 4.12) where the vortices goes through. The spectrums are computed from the data series of the water surface elevation in the indicated point.

PANS with $f_k = 1.0$ (Fig. 5.3(a)) presents a spectrum where the mid energy peak corresponds to a frequency value close to 0.2Hz and it is related with the vortex shedding frecuency. PANS $f_k = 0.8$ (Fig. 5.3(b)) has a larger energy associated to 0.2Hz. Thus, vortices have more kinetic energy. In PANS with $f_k = 0.6$ (Fig. 5.3(c)) and with $f_k = 0.4$ (Fig. 5.3(d)) the energy of the 0.2Hz

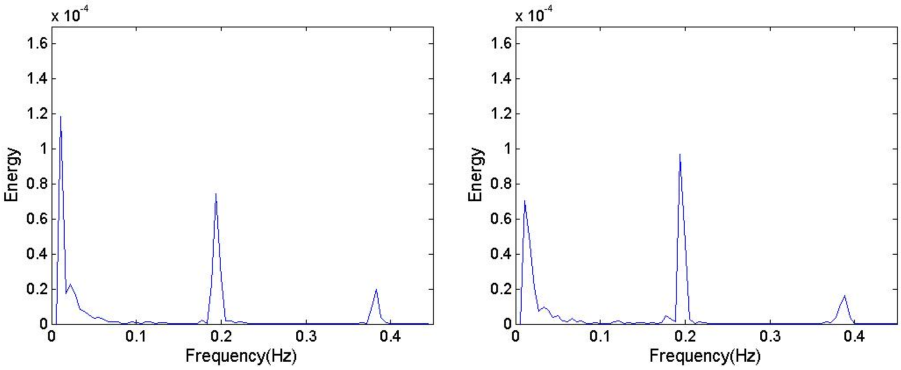

(a) PANS $f_k = 1.0$

(b) PANS $f_k = 0.8$

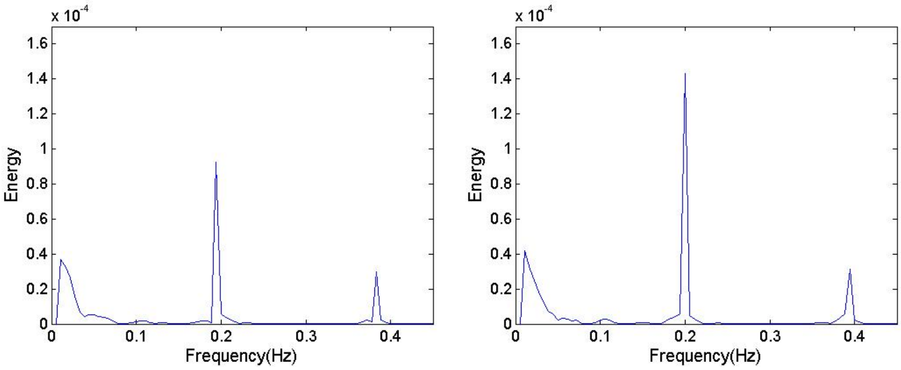

(c) PANS $f_k = 0.6$

(d) PANS $f_k = 0.4$

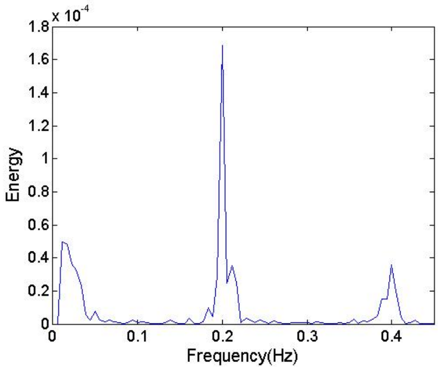

(e) PANS $f_k = 0.2$

Figure 5.3: Energy-frequency spectrums in PANS simulations. The reference point is the x=1.17m y=-0.1m (Fig.4.12)

frequency becomes larger as the resolved turbulence is larger.

In PANS with $f_k = 0.2$ (Fig. 5.3(e)) the spectrum achieves a high energy value for the shedding frequency (0.2Hz). As the resolved turbulence is increased, the vortices gain energy and this is reflected in the energy contained in their shedding frequency. The energy values for this frequency is more than twice for PANS with $f_k = 0.2$ than with $f_k = 1.0$.

Turbulent kinetic energy

Table 5.3 shows the value of the time and space averaged turbulent kinetic energy during 100s.

f_k	Modelled total kinetic energy	Resolved total kinetic energy
1.0	$2.02027 \cdot 10^{-2}$	$1.5320 \cdot 10^{-2}$
0.8	$2.01695 \cdot 10^{-2}$	$1.5853 \cdot 10^{-2}$
0.6	$2.00615 \cdot 10^{-2}$	$1.4613 \cdot 10^{-2}$
0.4	$2.00596 \cdot 10^{-2}$	$1.5082 \cdot 10^{-2}$
0.2	$2.00529 \cdot 10^{-2}$	$1.6789 \cdot 10^{-2}$

Table 5.3: PANS comparison of time and space averaged turbulent energies.

The results from $f_k = 1.0$, 0.8 and 0.2 are as expected, the resolved turbulent kinetic energy increases as f_k disminishes, but the results of f_k=0.6 and 0.4 are not. In order to analyze the result focus only on the flow downstream the cylinder, results from a horizontal line (Fig.5.4) are obtained. The resolved kinetic energy obtained from this line is plotted in Fig. 5.5. The results show the expected evolutionof the resolved kinetic energy values with the PANS models. At x=0.25m the peak values of the resolved kinetic energy are larger as f_k disminishes.

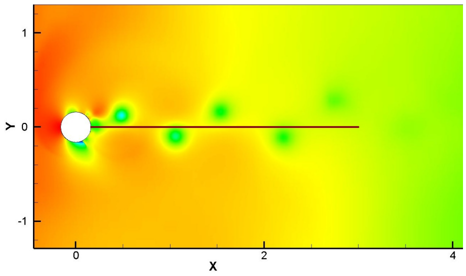

Figure 5.4: Location of the line used for analyze variable profiles. Water surface elevation represented.

Fig. 5.6 shows that PANS with f_k=0.4 and 0.2 produce less modelled kinetic energy wherein the turbulence is important (from x=0.25m to 0.5m). The largest differences are in the beginning, as PANS with f_k=0.6, 0.4 and 0.2

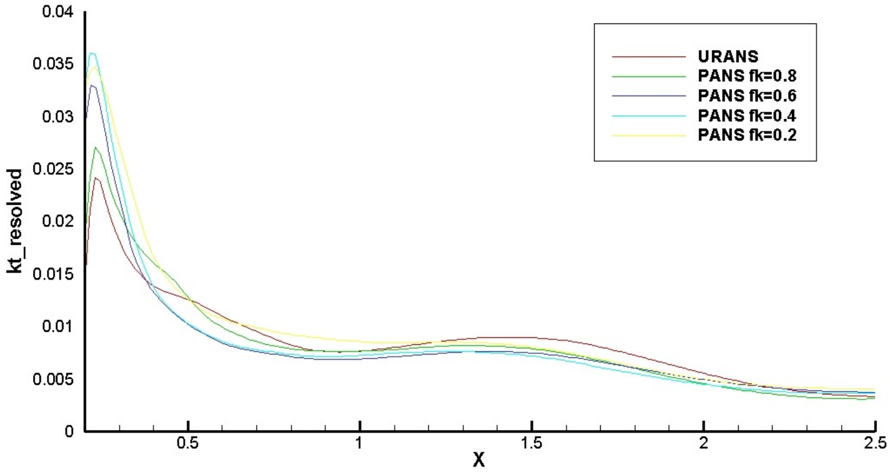

Figure 5.5: PANS resolved kinetic energy comparison along the considered straight line (Fig.5.4).

achieve similar values from x=0.4m. However, URANS and PANS with f_k=0.8 results differ from the one achieved by the previous until x=1m where all the models have similar results. This analysis stablishes that as f_k diminishes, the resolved turbulence is larger only where the turbulence is relevant, as within the vortex street. The rest of the domain is resolved with similar results in all PANS models.

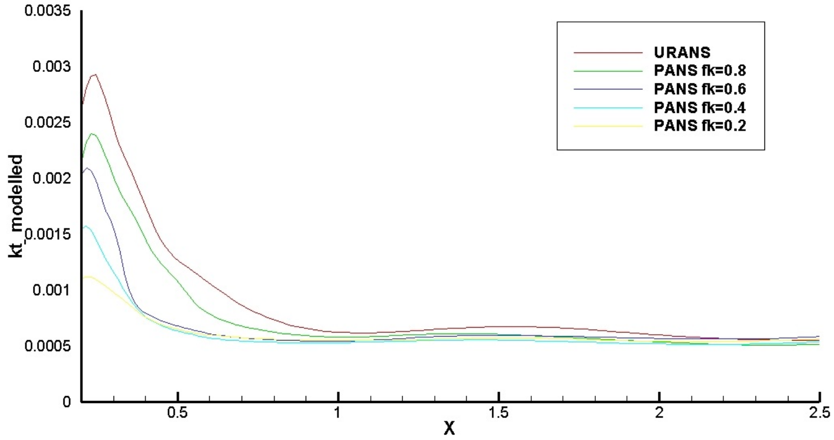

Figure 5.6: PANS modelled kinetic energy comparison along the considered straight line (Fig.5.4).

Variable profiles

Several profiles are used to analyze the differences on kinetic energies and velocity values. This profile is situated at X=1m, and it extends from Y=0.3m down to Y=-0.3m (Fig. 4.3).

Fig. 5.7 represents the horizontal velocity in all the PANS simulations. PANS with $f_k = 1.0$ achieves the largest mean velocity at Y=0m (lowest velocity deficit) and the profile is perfectly symmetric. However, the rest of PANS simulations are not exactly symmetric. This is probably because the time average during 100 seconds have not completely achieved convergence.

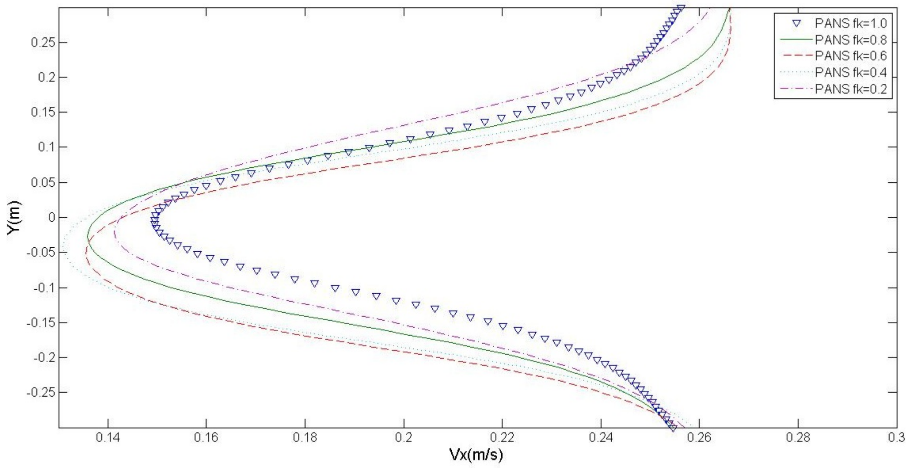

Figure 5.7: Horizontal velocity profiles in PANS turbulence model comparison

The resolved term of the kinetic energy is related with the vorticity of the vortices. This energy has to be larger in the regions where the vortices pass through, as seen in the figures of vortex streets contours (Figures from 5.1(a) to 5.1(e)). In Fig. 5.8 PANS with f_k lower than 1.0 have profiles where the maximum values of resolved turbulent kinetic energy are achieved where vortex cores pass through. URANS simulation does not present this pattern, it simulates the largest resolved kinetic energy in the center of the region where the vortices cores do not pass through. The inverse relation between the modelled and the resolved kinetic energies is appreciated in Fig. 5.9 and 5.8.

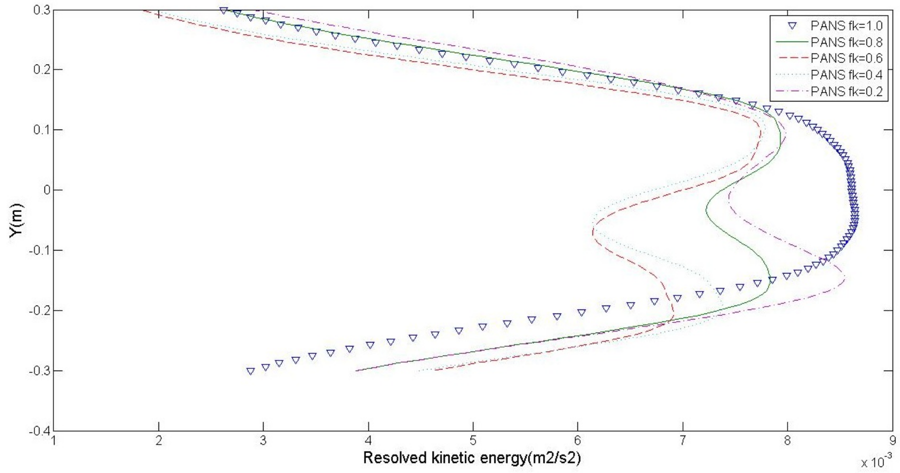

Figure 5.8: Resolved kinetic energy in PANS turbulence model comparison

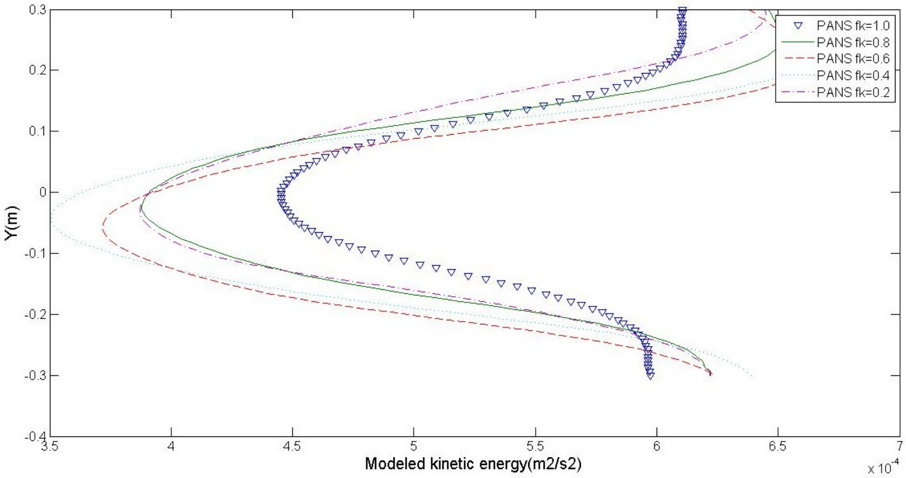

Figure 5.9: Modelled kinetic energy in PANS turbulence model comparison

5.3 Filter-based URANS

The FB model offers a filtering system more physical in the sense that the filter is related to the smallest instabilities that we want to resolve. FB model filter does depend on the mesh element size, as defined in Eq. 1.22.

Concerning turbulence kinetic energy, the smaller the filter is, the larger the resolved kinetic energy is. At the same time, a smaller filter means that the modelled kinetic energy is lower.

The cases analized with the filter-based URANS model are presented in Table 5.4.

Filter size ($\triangle$)	Related value
0.05m	2*h
0.025m	h
0.016m	2*dx
0.0125m	h/2
0.008m	dx
0.00625m	h/4
0.004m	dx/2
0.002m	dx/4

Table 5.4: Filter-based URANS cases.

Vorticity

In this section Figures from 5.10(a) to 5.10(f) are compared in order to analyze the vorticity change when the filter size is decreased.

Figures 5.10(a) and 5.10(b) represent the vorticity of the simulations with the widest filters, $\triangle$=2h and h. The differences can be seen in the lastest vortices where the vorticity lines are larger in the filter $\triangle$=h than in 2h. Fig. 5.11 compares the vortices in both simulation.

In the cases where filter sizes are smaller than the mesh side (dx), as defined in this model, the filter can change in each mesh cell. In Fig. 5.10(c) there are some details that difference it from the wider filters. There are some small scale instabilities surrounding the third vortex. Also in Fig. 5.10(d) the tail has a different shape, with larger vorticity.

An interesting phenomenon is the small vortex or instability observed between the first and second vortices in Fig. 5.10(f). This is not simulated in any other simulation except in Fig. 5.10(e) where this kind of instability is observed downstream the cylinder (approximately close to the fifth vortex).

In order to show how the filter modifies the results, the comparison between Fig. 5.10(a) and 5.10(f) can be done. The coarse filter gives a vortex street with equidistant vortices and no small-scale instabilities. With the smallest filter the instabilities are more random, there is not a defined pattern in the shedding process and some small scale instabilities are simulated.

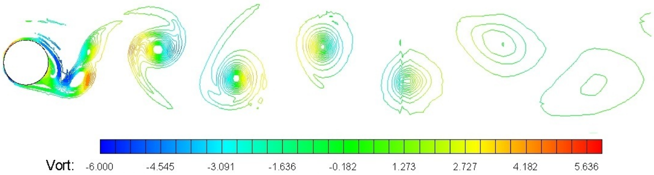

(a) △ = 2*h

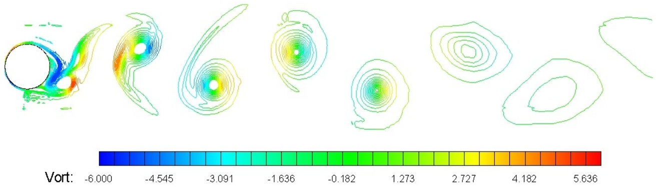

(b) △ = h

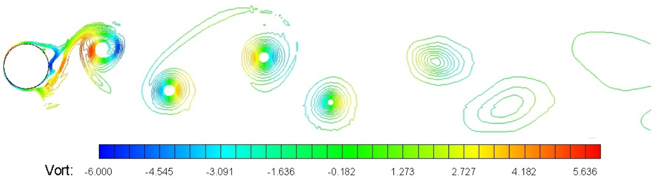

(c) △ = dx

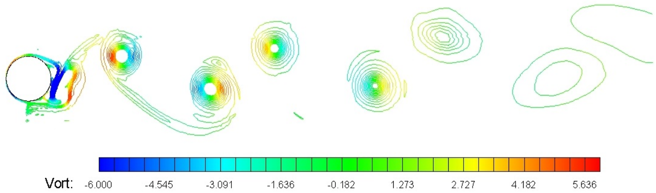

(d) △ = h/4

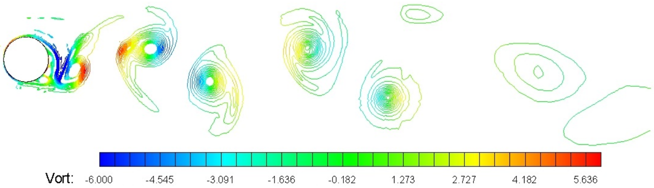

(e) △ = dx/2

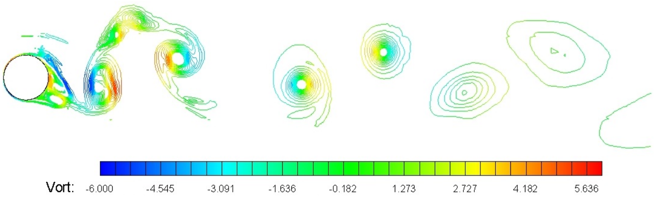

(f) △ = dx/4

Figure 5.10: Vorticity contour lines at t= 160s (t*=110) in FB simulations.

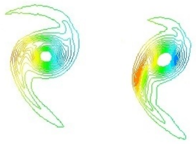

Figure 5.11: First shed vortex comparison between 2h and h filters.

Energy spectrum

Analogously to the PANS analysis, the energy-frequency spectrums, from the point represented in Fig. 4.12, are computed from the water surface elevation data. The behaviour of the spectrums with filters between $\triangle$=2h (Fig. 5.12(a)) to $\triangle$=h (Fig. 5.12(b)) is really similar to the PANS simulations from $f_k = 1.0$ to 0.4. The spectrums have three peak frequencies where the two first concentrate most part of the energy.

The change in the filtering begins with $\triangle$ = h/4 (Fig. 5.12(d)). The filter size is smaller than the mesh size so the filter changes in every cell. The result is a higher energy peak at 0.2Hz, which reaches an energy value of $3 \cdot 10^{-4}$. In FB with $\triangle$=dx/2 (Fig. 5.12(e)) the energy distribution approaches the spectrum from the filter $\triangle$=dx (Fig. 5.12(c)), with an energy distributed along a wider range of frequencies.

The spectrum from FB with $\triangle$=dx/4 is presented in Fig. 5.12(f). The spectrum has the largest energy associated to the 0.2Hz frequency, which corresponds with the vortex shedding frequency. There are many frequencies with low energy representing the turbulence increase that this filter has over h/4 or larger filters.

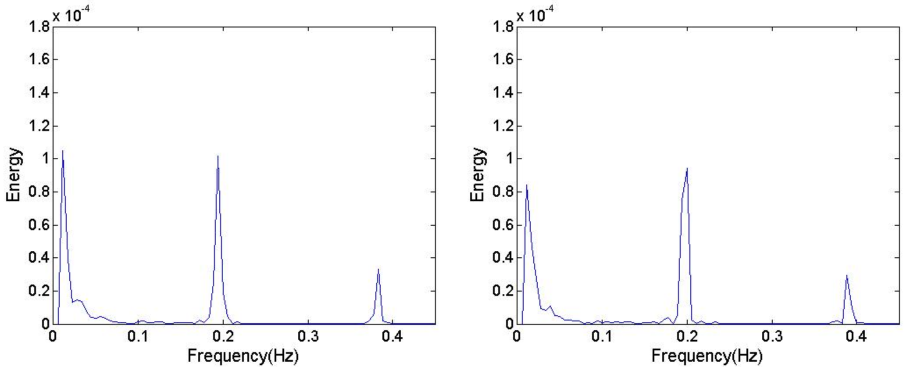

(a) △ = 2*h (0.05m)

(b) △ = h (0.025m)

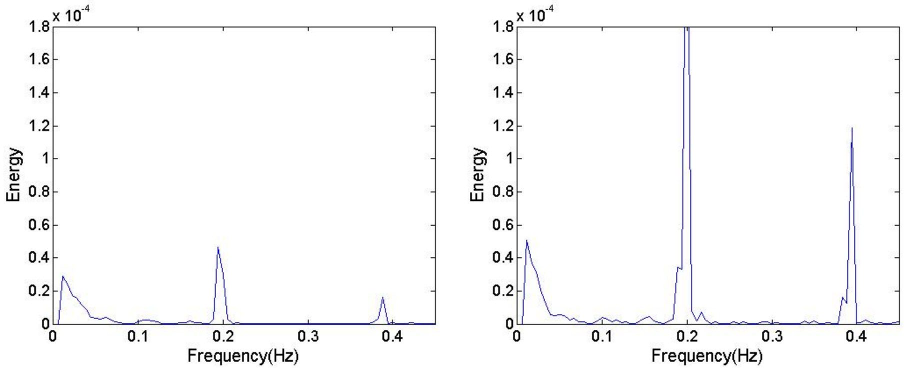

(c) △ = dx (0.008m)

(d) △ = h/4 (0.00625m)

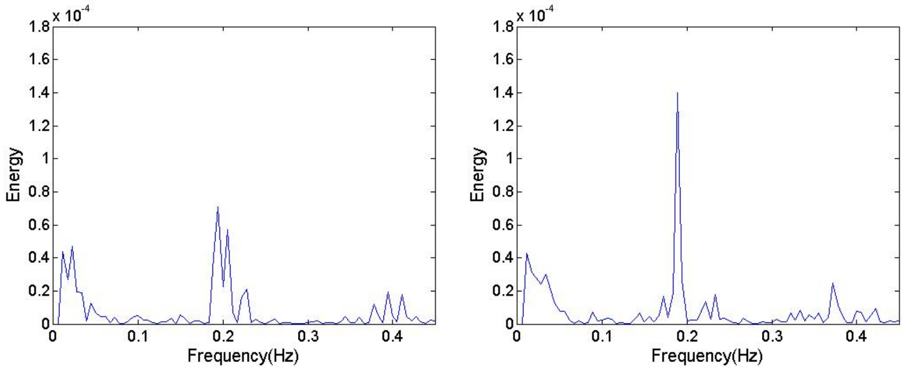

(e) △ = dx/2 (0.004m)

(f) △ = dx/4 (0.002m)

Figure 5.12: Energy-frequency spectrums of FB cases. The reference point is the x=1.17m y=-0.1m (Fig.4.12)

Turbulent kinetic energy

In Table 5.5 the modelled and resolved kinetic energies are integrated in the whole domain within a time range of 100s. On the one hand, the modelled kinetic energy has larger values as the filter is larger. On the other hand, the resolved kinetic energy does not present the expected evolution as it happened in PANS. While the smallest filters have the largest amount of resolved kinetic energy, the mid-size filters vary this kinetic energy term, without an increasing tendence.

Filter size (△)	Modelled total kinetic energy	Resolved total kinetic energy
2*h (0.05m)	$2.01903 \cdot 10^{-2}$	$1.53431 \cdot 10^{-2}$
h (0.025m)	$2.01530 \cdot 10^{-2}$	$1.59067 \cdot 10^{-2}$
2*dx (0.016m)	$2.00913 \cdot 10^{-2}$	$1.52892 \cdot 10^{-2}$
h/2 (0.0125m)	$2.00157 \cdot 10^{-2}$	$1.40792 \cdot 10^{-2}$
dx (0.008m)	$1.99820 \cdot 10^{-2}$	$1.42697 \cdot 10^{-2}$
h/4 (0.00625m)	$1.99857 \cdot 10^{-2}$	$1.46367 \cdot 10^{-2}$
dx/2 (0.004m)	$1.99976 \cdot 10^{-2}$	$1.74381 \cdot 10^{-2}$
dx/4 (0.002m)	$2.00122 \cdot 10^{-2}$	$1.91174 \cdot 10^{-2}$

Table 5.5: FB simulations comparison of integrated values turbulence energies.

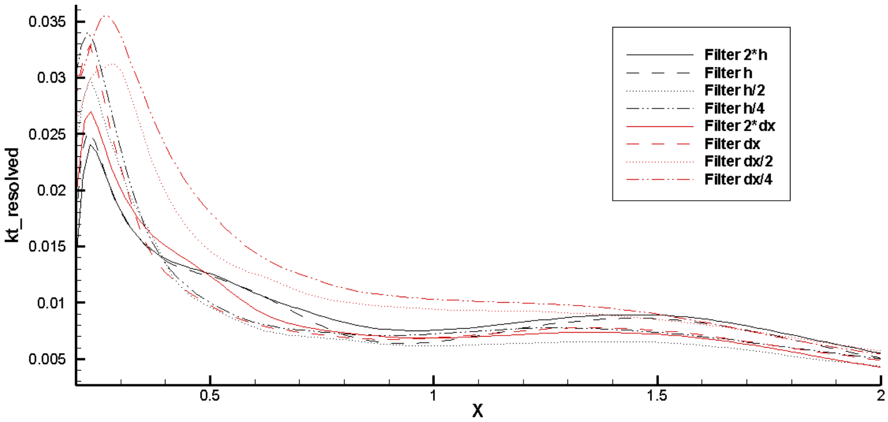

Figure 5.13: Filter-based URANS resolved kinetic energy comparison along the considered straight line (Fig. 5.4).

Fig. 5.13 and 5.14 show respectively the longitudinal profile, obtained from the line in Fig. 5.4, of the resolved and modelled turbulent kinetic energy. In Fig. 5.13 the smallest filter reaches the largest values of resolved turbulent kinetic energy and the largest filter reaches the smallest values. The intermediate filters follow the expected behaviour. The largest filter results are really close to the URANS results. Far from the cylinder all the filters resolves approximately the same amount of resolved kinetic energy, as it can be seen at x=2m. This reflects the filtering only affects to the high instability regions close to the cylinder, where the turbulence is important.

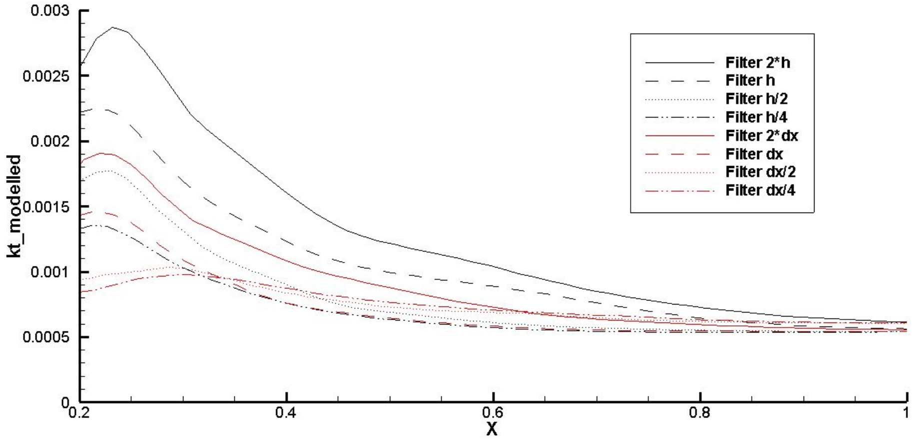

Figure 5.14: Filter-based URANS modelled kinetic energy comparison along the considered straight line (Fig. 5.4).

The profile of the resolved turbulent kinetic energy values along the reference line (Fig. 4.3) is presented in Fig. 5.15 and 5.16. All filter sizes has a resolved kinetic energy disfribution as PANS results (Fig. 5.8). The smallest filters $\triangle$=dx/2 and dx/4 have a different profile, with values larger than any other filter case but keeping the two-peak profile.

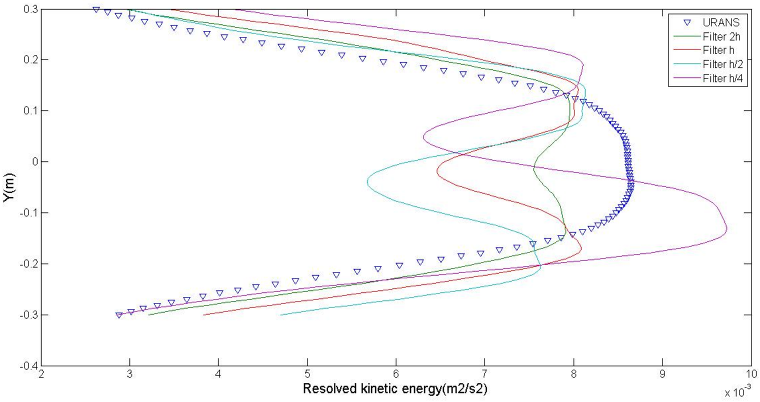

Figure 5.15: Filter-based URANS resolved kinetic energy comparison.

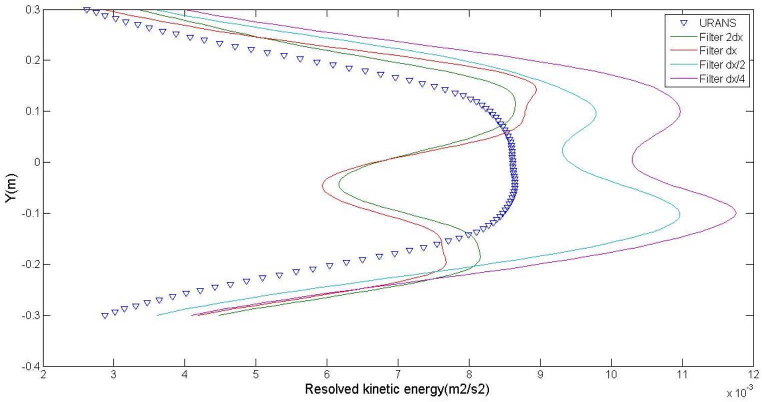

Figure 5.16: Filter-based URANS resolved kinetic energy comparison.

5.4 Eddy viscosity

A difference between the turbulence models used in this work is how the turbulent viscosity is computed. The equations that are used in each turbulence model to calculate the turbulent viscosity are:

- URANS.

$$\nu_t = C_\mu \frac{k^2}{\varepsilon}$$

- PANS.

$$\nu_u = C_\mu \frac{k_u^2}{\varepsilon_u}$$

- Filter-based URANS.

$$\nu_t = C_\mu f \frac{k^2}{\varepsilon} \qquad\qquad f = min[1, C_3 \frac{\triangle \varepsilon}{k^{3/2}}]$$

Fig. 5.17(a) and 5.17(b) represent the instantaneous turbulent viscosity of URANS and FB ($\triangle$=h) models. Downstream the cylinder, the first vortices have the largest amount of turbulent viscosity in comparison with the rest of the vortices. Fig. 5.17(c) shows the values for PANS with f_k=0.6 where the situation is different from the two previous, the large viscosity zones (red zones) are now reduced. The turbulence increases in FB with $\triangle$ = dx (Fig. 5.17(d)) and PANS with f_k = 0.2 (Fig. 5.17(e)) and the turbulent viscosity disminishes now its value considerably.

The drag and lift coefficients show the oscillating pattern of the vortex shedding. Fig. 5.18 and 5.19 show the behaviour of these coefficient for several turbulence models. PANS with f_k=1.0 and FB with $\triangle$=h have an uniform lift coefficient oscillation in comparison with PANS with f_k = 0.6 and FB with

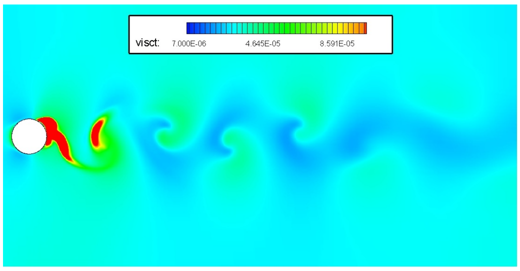

(a) URANS

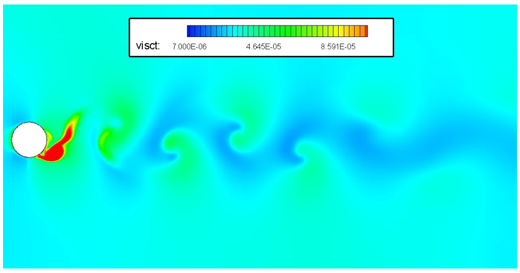

(b) Filter-based URANS △ = h

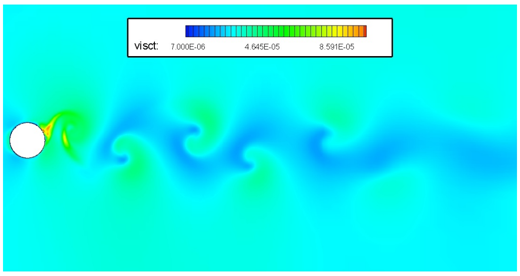

(c) PANS $f_k = 0.6$

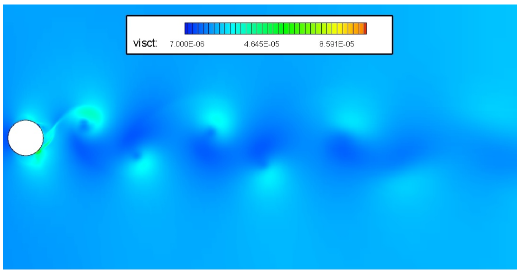

(d) Filter-based URANS △ = dx.

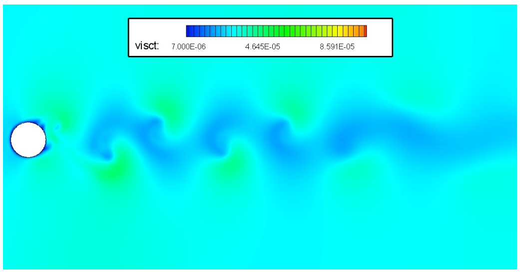

(e) PANS $f_k = 0.2$

Figure 5.17: Instantaneous turbulent viscosity field

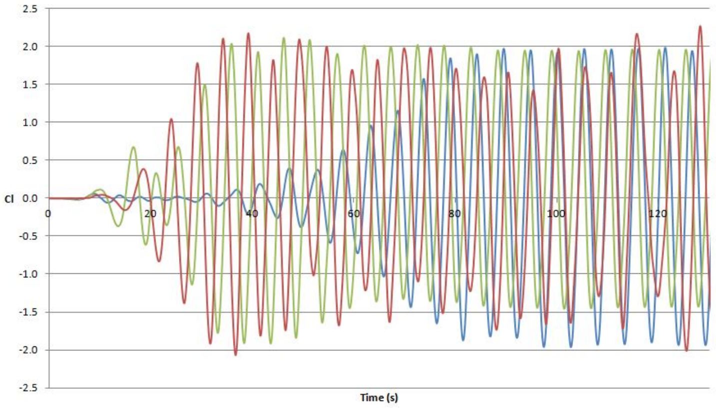

Figure 5.18: PANS lift coefficient comparison. f_k = 1.0 (blue), f_k = 0.6 (green) and f_k = 0.2 (red).

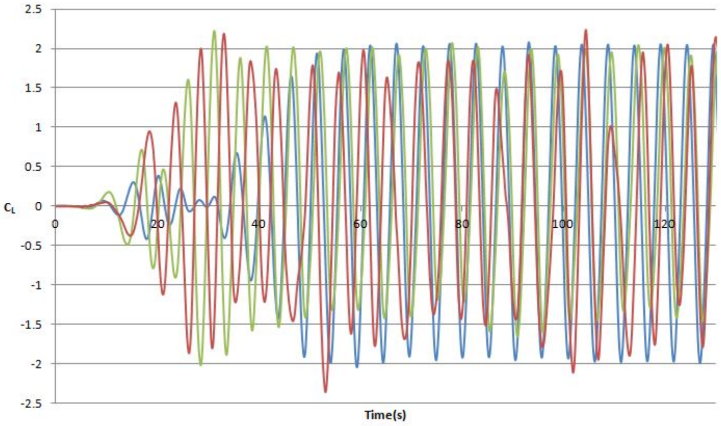

Figure 5.19: Filter-based URANS lift coefficient comparison. △ = h (blue), △ = dx(green) and △ = dx/4 (red).

△=dx as their lift coefficient is not uniform, due to the lack of symmetry or different amplitude along time. In the last two cases the oscillation starts sooner than in the first ones, and after a certain time period the oscillation is stabilized, but this is not uniform.

In PANS with f_k = 0.2 and FB with △ = dx/4 the period of the lift coefficient cycles is random. Indeed, in the FB case the vortex frequencies range is more broader than in PANS. The result of this is reflected in Fig. 5.12(f), where there are a huge range of frequencies with an appreciate quantity of energy, in comparison with Fig. 5.3(e) where there are just three main frequencies.

In Fig. 5.20 and 5.21, the turbulence models among the considered ones that resolve less turbulent energy (PANS with f_k=1.0 and FB △=h) have an uniform oscillation of the drag coefficient.

Between PANS with $f_k = 0.6$ and FB with $\triangle$ = dx there are not so many differences. The amplitude in the drag coefficient oscillation of these models is larger more than the achieved by the $f_k = 1.0$ and $\triangle$ = h. This indicates that the vortices are stronger, and the force over the cylinder is larger, as the vortex suction provokes drag.

The drag coefficient oscillation for PANS with f_k=0.2 and FB with $\triangle$=dx/4 is as random as the lift coefficient. The PANS case simulation has a drag coefficient that oscillates within 2.0 and 1.5, but there are peaks where the drag reaches larger values. Otherwise, the FB case has a drag coefficient behaviour without any pattern, reaching different values over time.

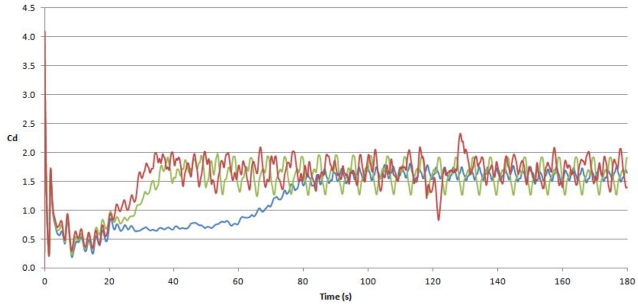

Figure 5.20: PANS drag coefficient comparison. f_k = 1.0 (blue), f_k = 0.6 (green) and f_k = 0.2 (red).

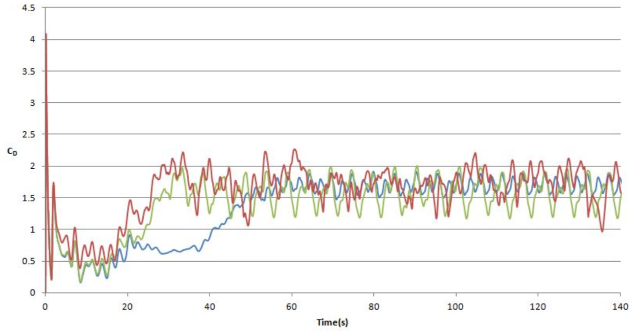

Figure 5.21: Filter-based URANS drag coefficient comparison. $\triangle$ = h (blue), $\triangle$ = dx(green) and $\triangle$ = dx/4 (red).

5.4.1 Vorticity comparison

The numerical scheme and the turbulence model have a big influence in the numerical results. Fig. 5.22(a) shows the vortex shedding as a result from Chen and Jirka experiments [8]. Fig. 5.22(b) shows the result of the vortex shedding obtained from our numerical simulation with URANS turbulence model and

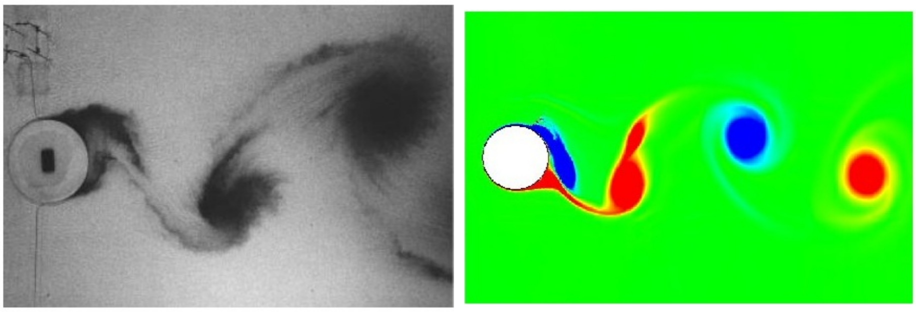

(a) Experimental

(b) URANS

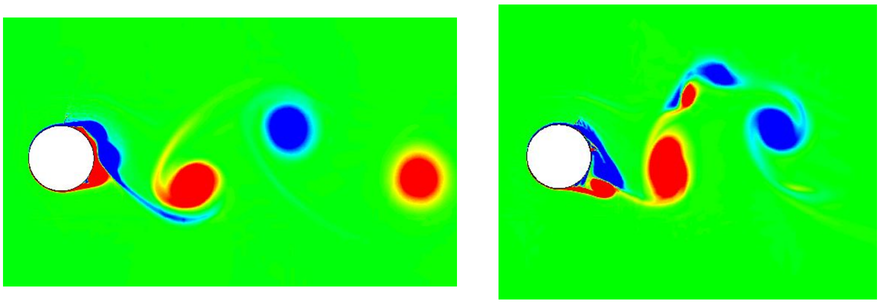

(c) PANS

(d) Filter-based URANS

Figure 5.22: Vortex shedding comparison between experimental and our numerical results.

using the Roe numerical scheme. PANS with f_k=0.2 result with the HLLCC numerical scheme is presented in Fig. 5.22(c). The vortex shedding from the filter-based URANS with a filter size of $\triangle$=dx/4 using the HLLCC numerical scheme, is shown in Fig. 5.22(d).

Conclusions

The CFD simulations in shallow water flow using depth-averaged models show a good agreement with experimental observations. The CFD results depend on the numerical mesh, turbulence model and numerical scheme. These three factors will determine how close are the results between the experiments and the CFD.

The CFD simulations were compared with experimental data in order to study if they can simulate the vortex street, unsteady bubble or steady bubble downstream the bluff bodies. The CFD model reproduces satisfactory the phenomena in the flat plate case, as all the instability types are correctly reproduced. In the circular cylinder case, the model has problems in cases where the Froude number is low.

A proper numerical scheme might be chosen to study the flow around bluff bodies in shallow waters. Standard schemes as the HLL or the Roe schemes have an excessive numerical diffusion for unsteady simulations as they were designed for standard RANS modelling. However, numerical schemes with a lower diffusion, such as the HLLCC or the Upwind-HLL, might be more appropiate to simulate the unsteady flow around bluff bodies. The schemes with higher numerical diffusion damp the turbulent oscillations.

The turbulence model used determines how much turbulence is simulated. The $k-\varepsilon$ model from URANS equations is the simplest turbulence model used in this document. In PANS and filter-based URANS the amount of resolved turbulent kinetic energy is dependent on the filter applied. The resolved kinetic energy is increased in the zones where the turbulence is relevant, as downstream the bluff body where the vortices are formed and shed. Concerning the modelled kinetic energy, this is reduced in the turbulent zones, being the URANS values the highest ones. The difference between PANS and filter-based URANS is that the last one resolves all the instabilities larger than the filter size set. Meanwhile, PANS simulation resolves a percentage of the total kinetic energy and therefore the highest level of resolved turbulence occurs in the vortex cores as they are the zones where the energy of the vortices is larger.

Filter-based URANS behaves differently depending on the filter value. If the filter size has a value close to the water surface elevation (h), the results approaches the URANS turbulence model. However, with a filter size close to the mesh element size (dx), the turbulence is more random and small-scale instabilites are solved.

As future lines of investigation, both the low diffusion numerical schemes and the turbulence models of PANS and filter-based URANS have to be compared with other experimental data to conclude which model is the most accurate. In order to resolve turbulent eddies smaller than the water depth, 3D models should be used. Comparison of the results given by 3D and 2D models would allow to assess the relevance of resolving the small scale eddies (smaller than h) The flow around bridge piles, river flows, seawalls or flow in harbours are some of the problems in shallow waters that can be simulated with these turbulence models, in order to study phenomena as scour, particle dispersion, etc.

References

[1] Wendt, J.F: *Computational Fluid Dynamics, An introduction.* A Von Kármán Institute book. 1991.

[2] Verteeg, H.K.,Malalasekera, W.: *An introduction to Computational Fluid Dynamics. The Finite Volume Method.* Pearson Prentice Hall. 2007.

[3] Davidson, L.: *Fluid mechanics, turbulence flow and turbulence modelling.* Chalmers Technical University. 2012.

[4] Davidson, L.: *An introduction to Turbulence Models.* Chalmers Technical University. 1997.

[5] Cea, L.: *An unstructured fnite volume model for unsteady turbulent shallow water flow with wet-dry fronts: Numerical solver and experimental validation.* University of A Coruña. 2005.

[6] Cea, L., Puertas, J., Vzquez-Cendn, M.E: Depth averaged modelling of turbulent shallow water flow with wet-dry fronts. *Archives of Computational Methods in Engineering, State of the art reviews*, Vol.14 (3) pp.303-341, 2007

[7] Roe, P. L. Discrete models for the numerical analysis of time-dependent multidimensional gas dynamics. *J. Comput. Phys.* 63, 458-476 1986.

[8] Chen, D.,Jirka, G.H.: Experimental study of plane turbulent wakes in a shallor water layer. *Fluid Dynamics Research* 16, 11-41. 1995.

[9] Monkewitz, P.A.: The absolute and convective nature of instability in two-dimensional wakes at low Reynolds number. *Phys. Fluids* 31(5), 999-1006. 1988.

[10] Tonui, N., Sumner, D.: Flow around impulsively started square prisms. *Journal of Fluid and Structures* 27, 62-75. 2011.

[11] Young, M.E., Ooi, A.: Comparative Assessment of LES and URANS for Flow Over a Cylinder at a Reynolds Number of 3900. 16^{th} *Australian Fluid Mechanics Conference.* 2007.

[12] Ma, J.M. et al.: A low Reynolds number variant of partially-averaged Navier-Stokes model for turbulence. *Int. J. Heat Fluid Flow.* 2011.

[13] Girimagi, S. et al.: Partially Averaged Navier-Stokes Method for turbulence: Fixed Point Analysis and Comparison with Unsteady Partially Averaged Navier-Stokes. *Journal of Applied Mechanics* 73. 2006.

[14] Johansen, S.T. et al.: Filter-based unsteady RANS computations. *Int. J. Heat Fluid Flow.* 2003.

[15] Charbeneau, R.J., Holley, E.R.: *Backwater effect of bridge piers in subcritical flow.* Texas Department of Transportation. University of Texas at Austin. 2001.

[16] LaRose, G.: *Notes from Calculus I*, Nebraska Wesleyan University. 1997.

[17] Li, L., Yan, Z., Liu, Z.: Numerical Model for Shallow Water behind Cylinder. *Applied Mechanics and Materials* Vols. 212-213, 1205-1212. 2012.

[18] Ramirez, L.: *Nuevas familias de métodos de volúmenes finitos de alto orden basados en formulaciones meshless para aplicaciones en mecánica de fluidos computacional* . Universidade de A Coruña, 2012.